https://doi.org/10.5194/egusphere-2026-4367
Preprint. Discussion started: 12 August 2026

Analytical improvements and a machine-learning assessment of age dispersion in laser-ablation (U-Th)/He zircon dating

Maximilian K. Ehrenfels[1], Daniel F. Stockli[1], Richard A. Ketcham[1], Desmond B. Patterson[1], and Michael G. Prior[1]

[1]Department of Earth and Planetary Sciences, Jackson School of Geosciences, University of Texas at Austin, Austin, 78712, Texas, USA

Correspondence: Maximilian K. Ehrenfels (max.ehrenfels@utexas.edu)

Abstract. Laser-ablation (U-Th)/He dating offers major advantages over conventional whole-grain dissolution analysis, including spatially resolved sampling, minimal sample preparation, and much faster data acquisition. Despite these advantages, the method's full potential is held back by issues including the lack of standardized, fully documented analytical protocols, and age dispersion that commonly exceeds the propagated analytical uncertainty. In this study, we document a complete LA-(U-Th)/He workflow for zircon, combining ultra-high-vacuum laser extraction, white-light-interferometric pit-volume measurement, and time-resolved LA-ICP-MS parent-nuclide quantification, and introducing two methodological refinements: a dynamic multi-phase oxide normalization for the parent concentration calculation, and parent-source depth weighting to account for alpha redistribution. Applied to 811 spots in Fish Canyon Tuff (FCT) zircon, the workflow yields a median age of 28.32 Ma (σ_{MAD} = 3.85 Ma; 13.6 %), in agreement with the published reference age, and reduces dispersion by a factor of ∼1.7 relative to conventional ^{29}Si- or ^{91}Zr-based reductions. To identify the drivers of the remaining dispersion, we train a gradient-boosted regression model on 33 simultaneously measured per-spot parameters. He pit volumes emerge as the strongest predictor of age residuals, highlighting volume-correlated analytical and geometric effects as the largest identifiable and potentially correctable source, while elevated ^{208}Pb concentrations flag inclusion-related disturbance and provide a practical spot-screening criterion. The measured degree of zonation within the ICP-MS profile on the other hand carries no independent predictive information. Instead, a simple two-layer zonation model shows that U-Th zonation in the grain volume removed during polishing can alone generate age offsets exceeding the entire residual dispersion, a mechanism confirmed by the contrast in dispersion between zoned FCT zircon (13.6%) and the compositionally homogeneous LGC megacryst (1.5%). The residual dispersion is therefore not an instrumental limitation, and further gains in precision will require a new generation of methods that characterize or circumvent the polished-away parent-source volume.

1 Introduction

Over the past three decades, (U-Th)/He dating, which relies on the emission of α-decay of U, Th, and Sm, has become a well-established and widely applied low-temperature thermochronometer (e.g., Zeitler et al., 1987; Farley, 2002; Reiners, 2005). Conventional single-grain analyses, however, are complicated by time-intensive sample preparation, the handling of toxic acids,

https://doi.org/10.5194/egusphere-2026-4367
Preprint. Discussion started: 12 August 2026

the necessity of α-ejection corrections, and the requirement for pristine, inclusion-free crystal morphologies. In most other isotopic systems, many of these constraints were overcome by laser-ablation (LA), which since its introduction in the 1980s has enabled spatially resolved sampling of nanogram-scale volumes directly from mineral grains without chemical dissolution (Gray, 1985; Fryer et al., 1993; Horn et al., 2000). LA-ICP-MS in particular has become the dominant approach for U-Pb geochronology and detrital provenance studies (Košler and Sylvester, 2003; Gehrels et al., 2008), and laser-based extraction is routine in $^{40}Ar/^{39}Ar$ thermochronology (Kelley et al., 1994; Wartho et al., 1999; Kramar et al., 2001; Hodges et al., 2005). In principle, the same promise holds for (U-Th)/He: Since its first demonstration on monazite by Boyce et al. (2006), laser-ablation has been shown to overcome many of the limitations of conventional whole-grain analysis while producing statistically indistinguishable ages. Subsequent studies since then have refined nearly every component of the analytical workflow and extended the method to apatite (Horne et al., 2019; Pickering et al., 2020) and zircon (Vermeesch et al., 2012; Tripathy-Lang et al., 2013; Evans et al., 2015). More recent work has also explored whether LA-(U-Th)/He datasets can constrain continuous thermal histories (Glotzbach and Ehlers, 2024; Maier et al., 2026). Despite these methodological advances over the past 20 years, laser-based (U-Th)/He has so far seen only limited adoption.

At least partially responsible are the issues still plaguing it. The first is that LA-(U-Th)/He datasets typically display age dispersion substantially in excess of the propagated analytical uncertainty (Hodges et al., 2021; Vermeesch et al., 2023; Léger et al., 2023). "Overdispersion" is also documented in conventional dissolution datasets, where it has been attributed to U-Th zonation and the resulting α-ejection bias (Hourigan et al., 2005; Dobson et al., 2008), uncertainties in the FT corrections (Ketcham et al., 2011), and the presence of mineral or fluid inclusions, parentless He, or defect-related He trapping (Vermeesch et al., 2007; Spiegel et al., 2009; Murray et al., 2014; Flowers et al., 2023b). In LA datasets, however, the dispersion is typically larger. Critically, the relative contribution of these proposed mechanisms to the total dispersion has never been quantitatively assessed, so it remains unknown which causes are correctable analytical effects, and which are inherent to the current setup of the method itself. A second major obstacle is the lack of methodological standardization: no analytical procedure comparable to the standardized protocols of conventional (U-Th)/He analysis (Flowers et al., 2023a) has been established for LA-(U-Th)/He, and the technical information required to set up such an analysis, such as UHV-compatible sample mounting, laser extraction, pit-volume determination, and in situ parent-nuclide quantification, remains fragmentary and scattered across the literature.

The primary focus of this study is twofold and addresses (1) an improved routine workflow for LA-(U-Th)/He dating and (2) quantification of analytical uncertainties using a machine-learning approach. We first document a complete LA-(U-Th)/He workflow developed at the UTChron laboratory at the University of Texas at Austin, that describes in reproducible detail sample mounting procedures, ablation pit profilometry and calibration, a dynamic multi-phase oxide normalization approach for parent concentration calculations, and a depth-weighted parent-source data reduction scheme. We apply and test this workflow to zircon standard materials (Fish Canyon Tuff and LGC) and use a gradient-boosted machine-learning regression model, trained on simultaneously measured per-spot parameters, to identify the principal physical and analytical drivers of the residual age uncertainty and dispersion.

https://doi.org/10.5194/egusphere-2026-4367
Preprint. Discussion started: 12 August 2026

2 Improved analytical workflow

For this study, we measured a total of 811 spots in zircons from the Fish Canyon Tuff (FCT), a widely used age standard with a reported zircon (U-Th)/He age of 28.3 ± 0.4 Ma (Gleadow et al., 2015). For comparison, we also compiled >700 zircon with conventional (U-Th)/He FCT ages acquired over several years at the UTChron Laboratory. We further measured 100 LA-(U-Th)/He ages from a shard ("LGC-3") of the Sri Lankan zircon metacryst LGC reference material (476.4 ± 5.7 Ma; Tian et al., 2017). While FCT zircon grains are characterized by α-ejection and internal parent nuclide zonation, LGC is an inclusion-free, unzoned, gem-quality megacryst, and therefore provides a fully independent test of both accuracy and internal precision of the method presented here. An overview of the complete analytical workflow is given in Fig. 1 and full technical details of each step are provided in Appendix A.

2.1 Mounting and polishing of grains

For laser-ablation He analysis, zircons need to be mounted and polished to expose internal surfaces that are not affected by α-ejection. Conventional epoxy mounting techniques, used for example for U-Pb dating, are not suitable for ultra-high vacuum (UHV) helium extraction, as they tend to outgas in the sample chamber and introduce substantially elevated blank levels and hydrocarbons and hydrogen contamination. For this reason, previous LA-(U-Th)/He studies have resorted to low-outgassing substrates such as TorrSeal (Horne et al., 2016), indium metal (Boyce et al., 2006; Vermeesch et al., 2012), PFA or FEP Teflon sheets (Evans et al., 2015; Pickering et al., 2020), or, more recently, tin-based alloy mounts (Hao et al., 2024).

For this study, we used transparent PFA Teflon and hot-pressed zircon grains into pre-flattened 8 mm PFA discs at 320 °C using an automated hot-press, ensuring for repeatable and consistent mounting. Zircons were co-mounted with Cospheric Soda Lime Solid Glass Microspheres (177.5 ± 2.5 µm) that serve as depth guides during subsequent polishing and removal of >20 µm to ensure removal of the alpha-ejection-affected rim zones. The exposed diameter of polished co-mounted glass microspheres provides an accurate measure of polishing depth following the procedure outlined by Pickering et al. (2020). We accomplished this by polishing for ∼3 min using a 6 µm diamond suspension, followed by 3 µm and 1 µm suspensions for ∼1 min each, and verification of final polishing depth by reflected-light microscopy. Up to four PFA Teflon mounts are attached to a custom-designed sample holder (Fig. 1, 1d; Appendix A, Fig. A1), which can be loaded both into our custom-designed UHV sample chamber and our ICP-MS sample cell.

2.2 Helium laser ablation measurement

LA-(U-Th)/He analysis critically depend on a laser-ablation system that is capable of producing clean, well-defined cylindrical pits that allow for accurate volume determinations. In addition, no He can be degassed from heating or thermal fracturing from the vicinity of the ablation pit. In this study, we employed a Teledyne Photon Machines Excite+ 193 nm ArF laser for in-vacuo He extraction with a nominal energy of 7.00 mJ, corresponding to a fluence of 11.38 J cm^{-2} and an energy of ∼0.75 mJ measured on the sample surface, after losses in the optical column and attenuation by the UHV chamber window. Routine zircon analyses were conducted using a 30 µm diameter spots, at 10 Hz repetition rate, and 100 to 200 total laser pulses. These

https://doi.org/10.5194/egusphere-2026-4367
Preprint. Discussion started: 12 August 2026

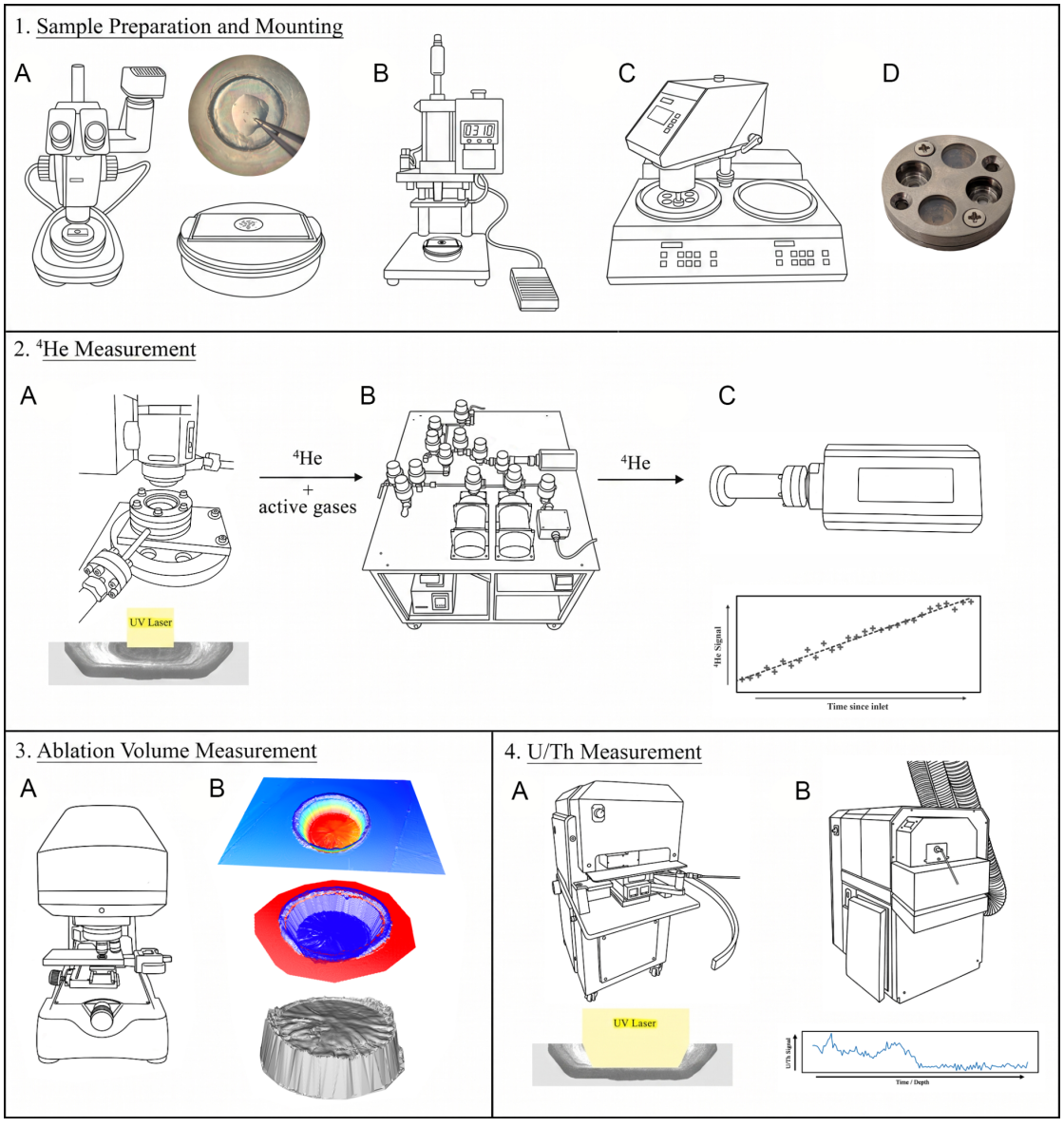

Figure 1. Protocol of laser-ablation (U-Th)/He dating developed in this study. 1.A) Grains are picked and loaded on a Teflon disk. B) Grains are pressed into the Teflon at 320 °C for 80 seconds at a pressure of 0.6 MPa. C) The Teflon disk is polished down ~20 microns. D) The Teflon disk is loaded into the sample holder. 2.A) Samples are loaded into a UHV sample chamber and pumped to $<10^{-9}$ mbar. A ~30 µm wide pit is ablated into the grain using an ArF excimer laser. B) The released gas is expanded into the line, where it is "cleaned" through the use of a getter and spiked with a known amount of 3He C) The He gas is measured in a quadrupole mass spectrometer. 3.A) To quantify the He signal, it is necessary to measure the volume of the ablated material using a white-light interferometer. B) The pit volume is extracted from the measured point cloud. 4.A) A second hole is ablated into the grain on top of the first using a similar ArF excimer laser. B) The released material is carried into an ICP-MS and the signal measured over time.

https://doi.org/10.5194/egusphere-2026-4367
Preprint. Discussion started: 12 August 2026

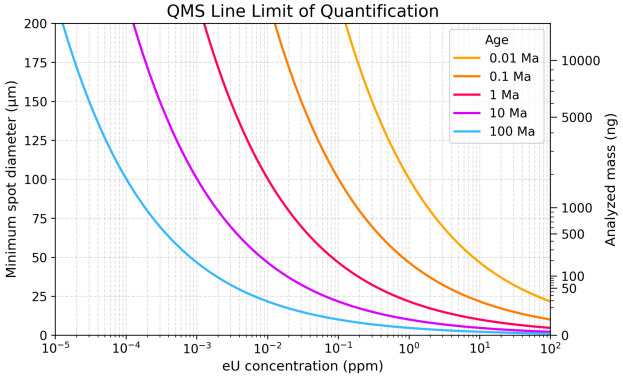

Figure 2. Minimum spot size required to produce a ^{4}He amount equal to the limit of quantification of the QMS line, calculated as a function of effective uranium concentration (eU) for ages between 0.01 and 100 Ma. Calculations assume a pit depth equal to one-half of the spot diameter.

settings resulted in an average ablation rate of ∼0.07 µm per shot, producing typical pit depths of 5–15 µm. Drill rates slightly decrease with depth, but this effect is negligible for <200 pulses.

Helium measurements were carried out following standard (U-Th)/He analytical procedures (Wolfe and Stockli, 2010). After in-vacuo sample ablation and inlet into the extraction line, the released gas (or blank) is spiked with ^{3}He for isotope dilution, purified on a SAES NP10 hot getter, and measured on a Pfeiffer Prisma 200 quadrupole mass spectrometer (QMS). Sample and blank ^{4}He concentrations were determined using interspersed spiked analyses of aliquots from a manometrically calibrated ^{4}He standard tank ("Q-tank"). Blank-corrected ^{4}He/^{3}He ratios of standard and unknown were used to quantify the ^{4}He amount of the sample. The full line configuration and measurement schedule are given in Appendix B. Sensitivity at these settings is ∼15.9 mol A^{-1}, with a mean blank level of 2.579 ± 0.058 × 10^{-16} mol. The limit of quantification (LOQ), which we define as $10 \times \sigma_{\mathrm{blank}}$, is therefore ∼0.58 × 10^{-16} mol, which is sufficient to quantify the helium release from a >10 µm ablation pit in a >1 Ma zircon with >10 ppm eU concentration (Fig. 2).

2.3 Ablation pit-volume measurement

Precise and accurate ablation pit volume determinations are paramount for robust LA-(U-Th)/He age determination. This is critical as even small geometric errors translate directly into He concentration biases and therefore age biases. Ablation pit volumes for LA-(U-Th)/He have mainly been measured by white-light interferometry (Boyce et al., 2006; Pickering et al., 2020), laser confocal scanning microscopy (Boyce et al., 2006; Wu et al., 2019), or atomic force microscopy (Evans et al., 2015; Danišík et al., 2017; Tian et al., 2017). For this study, the ablation pit volumes were measured using a Bruker ContourGT-K1 3D Optical Interferometer due to its fast data acquisition (∼10 s per pit) and high vertical resolution of ∼2 nm. Pits are scanned at a magnification of 60x, creating a 640 × 480 point cloud with a lateral resolution of 0.16 µm.

https://doi.org/10.5194/egusphere-2026-4367
Preprint. Discussion started: 12 August 2026

However, without adequate data evaluation and independent verification, the accuracy and precision of white-light interferometry data are hard to quantify, especially given the inability to image surfaces steeper than ∼60° or surfaces not directly in the path of light (Coupland and Lobera, 2010; Martínez Antón et al., 2015). We developed a fully-automated Python code that interpolates pit walls and extracts pit depth, diameter, volume, and their uncertainties from the interferometer point cloud. The algorithm is described in detail in Appendix B2. The code estimates a pit-specific analytical volume uncertainty by bootstrap resampling of the interferometry point cloud. This approach yields uncertainties of <1 % for most "clean" spots, to which a global systematic uncertainty of 2 %, based on repeated measurements of the same pits at different settings and angles, is added in quadrature. Final uncertainties are generally 2–5 %. Additionally, the code outputs an independently calculated pit depth, and a pit diameter.

In order to independently test the accuracy of our white-light interferometric volume measurements over a wide range of pit depths and diameters, we quantitatively compared ∼300 ablation pits in gem-quality Sri Lanka zircon against independently determined volumes derived from X-ray micro-computed tomography (µ-CT) images using a Zeiss Xradia 620 Versa scanned at a voxel resolution between 1.0 µm and 3.4 µm. Precise volumes were extracted from the dataset using the partial volume blurring (PVB) method (Ketcham and Mote, 2019) as implemented in the Blob3D software package (Ketcham, 2005). A more detailed description of our method can be found in Appendix C.

2.4 U and Th measurements

After in-vacuo He extraction and He ablation pit volume determinations, the sample holder puck is loaded into a Teledyne HelEx II sample cell connected to a Photon Machines Analyte G.2 ArF Excimer Laser for LA-ICP-MS determination of U and Th parent nuclide concentrations. The U-Th spot is positioned on top of the previously ablated He pit. The laser spot diameter is increased by 30–40 µm and the shot count adjusted to drill approximately 25 µm deeper than the He pit with a laser energy set at 6 mJ and a fluence of ∼2 J/cm^2 measured with an energy meter. This approach limits the practical minimum size of zircon grains that can be analyzed to ∼50 µm. The ablated sample aerosol is flushed using a He carrier gas and ionized using Ar plasma in a ThermoFisher Element2 sector-field HR-ICP-MS. The following elements are measured in the ICP-MS in peak-jumping mode: (1) The stoichiometric elements ^{29}Si, ^{91}Zr, and ^{178}Hf. (2) Stoichiometric elements of potential inclusions that could occur in our sample. In zircon these include ^{42}Ca for apatite, ^{49}Ti for titanite, ilmenite or rutile, ^{39}K for feldspar or biotite. (3) The parent isotopes ^{238}U and ^{232}Th. (4) Other trace elements of interest. (5) ^{235}U and Pb isotopes to allow U/Pb age determinations and (U-Th)/He-Pb double dating of detrital zircon samples. The NIST 610 glass (Jochum et al., 2011) is used as the primary concentration standard and interspersed throughout analytical sessions to correct for instrument drift. Given the potential impact of using non-matrix-matched glass standards on measurement accuracy (Kroslakova and Günther, 2007; Sylvester, 2008), we also measured secondary zircon standards AusZ2 (Kennedy et al., 2014) and LGC-3 (Tian et al., 2017) for quality control. We applied a standard downhole fractionation correction, based on time-resolved averaging the relative concentration profiles of each element in the secondary standards, to our unknowns.

https://doi.org/10.5194/egusphere-2026-4367
Preprint. Discussion started: 12 August 2026

2.5 Data reduction and age calculation

2.5.1 Helium

Raw helium mass spectrometry data were processed using a custom Python script to determine absolute He abundances by monitoring gas time-resolved gas evolution following gas expansion into the mass spectrometer and regressing to the time-zero intercept value. Final He concentrations (ncc) were quantified by normalizing ^{4}He/^{3}He ratios to a standard gas aliquot delivered from the reference tank. The baseline, interferences, and LOESS-based (Locally Estimated Scatterplot Smoothing) blank and sensitivity corrections, the correction for progressive depletion of the reference tank, and the propagation of uncertainties through all reduction steps are described in Appendix B1.

2.5.2 U-Th concentrations – oxide-sum normalization

Previous LA-(U-Th)/He studies have relied on the use of ablation pit volumes or internal standardization against stoichiometric mineral composition (Si or Zr) for the quantification of U, Th, and Sm. These approaches rely on a known density or concentration of the internal standard element in the analyzed material, respectively. Zircon density, however, can vary by up to 15% due to lattice damage (Holland and Gottfried, 1955), while the concentration of Si or Zr can vary due to lattice substitutions or the presence of inclusions. Ablating an inclusion could overestimate the calculated U-Th concentrations when using zircon density and severely over- or underestimate the calculated U-Th concentration when using Si or Zr as an internal standard (Fig. 3). To avoid the pit falls of simple stoichiometric normalizations, the quantification approach presented here instead builds on the oxide-sum normalization principle introduced for LA-ICP-MS by Halicz and Günther (2004), Guillong et al. (2005), Gagnon et al. (2008), and Liu et al. (2008). For this approach the concentrations of all major and trace elements were measured, converted to their respective oxide masses, and scaled to 100 wt.% sum. These scaled values were converted back to element concentrations, thus eliminating the need for explicitly known internal standard concentrations. Our approach follows a similar basic logic but adapts it for depth-profiling LA-ICP-MS in the context of zircon (U-Th)/He thermochronology. The key implemented adaptions are: (1) the use of a targeted element list used to fully reconstruct mineral stoichiometries rather than simple oxides, (2) no prior assumption of which mineral phase is being ablated at any given time step, enabling automatic handling of inclusions and mixed-phase ablation volumes, and (3) time-resolved application of both the sensitivity calibration and the normalization, yielding concentration-versus-depth profiles rather than bulk averages.

Hence, raw concentrations are calculated at each time step during depth-profiling from NIST 610-derived, drift-interpolated sensitivities, and each element is assigned a component factor f_i that converts the element mass to the mass of the full stoichiometric compound it represents in the expected mineral assemblage. At each time step, a "virtual" total component mass is then computed:

$$M_{\text{total}}(t) = \sum_{i=1}^{N} C_i^{\text{raw}}(t)\, f_i \tag{1}$$

The final scaled concentration of each element is then:

https://doi.org/10.5194/egusphere-2026-4367
Preprint. Discussion started: 12 August 2026

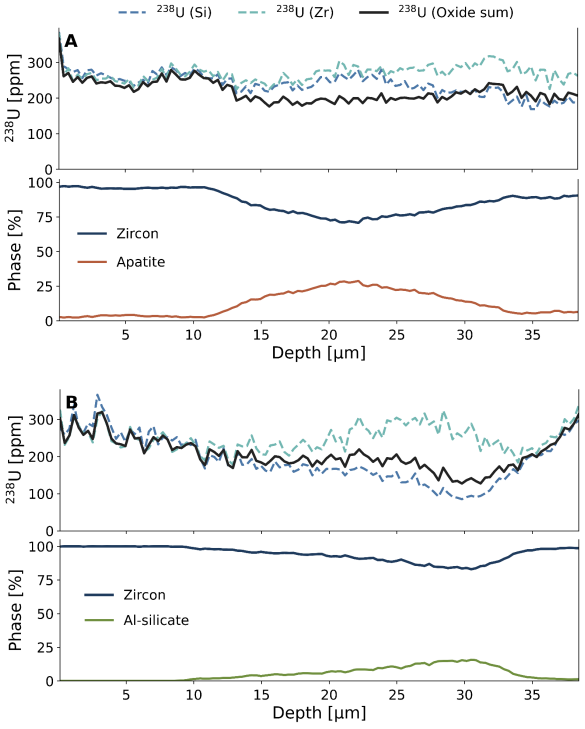

Figure 3. Example LA-ICP-MS depth profiles from a Fish Canyon Tuff zircon illustrating how mineral inclusions can bias internally standardized U concentrations. In profile A, the laser intersects an apatite, which contains U, but no stoichiometric Si or Zr, causing the apparent U concentration to be overestimated. Profile B intersects an Al-silicate inclusion, which contains only negligible amounts of Zr and U, but a higher stoichiometric Si concentration. As a result, the apparent U concentration is underestimated using Zr- and overestimated using Si-internal standards.

$$C_i^{\text{scaled}}(t) = C_i^{\text{raw}}(t)\frac{10^6}{M_{\text{total}}(t)} \tag{2}$$

where the factor 10^6 reflects normalization to 1,000,000 ppm (= 100 wt%). Importantly, this normalization does not require an assumption of which mineral is being ablated. Whether the laser is sampling only zircon, apatite or other mineral inclusions, or a mixed volume, the sum is simply the total of whatever components are present, and the normalization adjusts automatically. This further also allows for the quantification of nominal mineral phase proportions (e.g., "Zircon %", "Apatite %") at each time step, together with an "excess SiO_2" metric indicating free SiO_2 or, in the case of negative values, Si-free phases. The method is described in more detail in Appendix B3. The code also computes two zonation metrics for each parent nuclide and inclusion-indicator depth profile (U, Th, and Ca absolute concentrations): the "Zonation Magnitude", the ratio of the maximum to the minimum mean of statistically distinct zones within the profile, and the "zonation erraticness", the total variation between successive zone means divided by the overall amplitude range. A value near 1 means the profile changes mostly in one direction,

https://doi.org/10.5194/egusphere-2026-4367
Preprint. Discussion started: 12 August 2026

indicating simple rim-to-core enrichment or depletion, while higher values indicate a more oscillatory or patchy zoning pattern. The dynamic segmentation used to define the zones is described in Appendix B3.

2.5.3 U-Th concentrations – parent-source depth weighting

Most published in-situ (U-Th)/He methods generally treat the parent concentration as a simple average over the measurement volume, measured either by multiple SIMS or EPMA spots or by placing a larger LA-ICP-MS pit over the He pit (Boyce et al., 2006; Vermeesch et al., 2012; Tripathy-Lang et al., 2013; Evans et al., 2015; Pickering et al., 2020). The underlying assumption of these studies is that every parent atom within the ICP-MS measurement volume contributed equally to the measured He. The exact source region of ^{4}He, however, is governed by the alpha stopping distances of its parent isotope, which is not uniform across decay chains; in zircon, these range from approximately 5 µm for the single alpha emitted from ^{147}Sm to approximately 32 µm for ^{212}Bi in the ^{232}Th chain (Appendix B, Fig. B1; Ketcham et al., 2011). Even for a single stopping distance, the spatial distribution of parent source locations is not uniform but depends on the geometry of isotropic alpha emission into the cylindrical He pit volume, which produces a characteristic three-dimensional probability cloud (Fig. 4; Appendix B, Fig. B2). When, as is common practice in most LA-(U-Th)/He studies, the ICP-MS pit extends well beyond the He pit, the deep portion of the measured U-Th profile contributes little He to the shallow He pit yet receives equal weight in a simple average. This mismatch introduces a systematic bias that scales with the degree of compositional zonation in the grain.

In order to quantitatively determine the distribution of the parent atoms that produced the He measured in the extraction pit, we employ a reverse Monte Carlo simulation in which alpha-ejection trajectories are traced backwards from randomly sampled endpoints within the He pit, using the decay-chain-specific alpha energies and branching probabilities of Ketcham et al. (2011). The distribution of all parent locations forms a three-dimensional probability density cloud representing the spatial distribution of parents that contributed to the He pit (Fig. 4). As zonation in zircon is predominantly concentric about the c-axis, and grains are polished parallel to the c-axis and ablated perpendicular to the polished surface toward the grain center, the laser drills approximately perpendicular to the zonation shells, and concentration gradients within our ICP-MS volume are therefore predominantly a function of z. The parent endpoints are accordingly binned along z into a normalized depth-weighting density $w(z)$ at the depth resolution of the ICP-MS profile, and the depth-weighted parent concentration is obtained as:

$$C_{\mathrm{weighted}} = \int_{0}^{D_{\mathrm{ICPMS}}} C(z)\, w(z)\, \mathrm{d}z \tag{3}$$

where $C(z)$ is the measured concentration profile as a function of depth. In practice, a weighting curve is calculated for every measured spot using the values for He pit radius and depth obtained by the subsequent interferometer volume measurement.

2.5.4 Laser-ablation (U-Th)/He and U-Pb age calculation

Final LA-(U-Th-Sm)/He ages are calculated from the integration of the He concentrations, parent nuclide, and pit volume data. Absolute He abundances (ncc) and ablated pit volumes are first converted to atomic concentrations (atoms g^{-1}), assuming

https://doi.org/10.5194/egusphere-2026-4367
Preprint. Discussion started: 12 August 2026

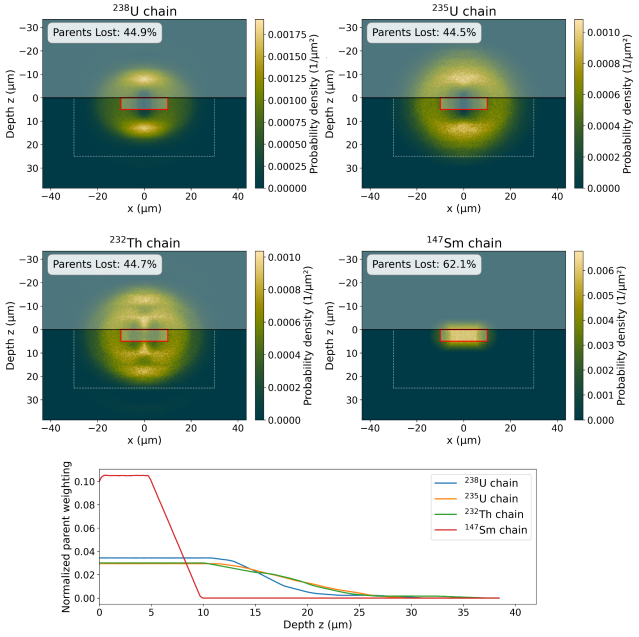

Figure 4. Cross-sectional (XZ) slices through 3D probability clouds of parent source regions for each of the four decay chains (^{238}U, ^{235}U, ^{232}Th, and ^{147}Sm), computed for a He pit of 20 µm diameter and 5 µm depth. The He pit is outlined in red, the grain surface is indicated as a solid black line, and the approximate extent of the ICP-MS pit is outlined as a dashed white line. "Parents Lost" refers to the percentage of parent atoms that are lost to the ICP-MS measurement due to their position in the polished-away section of the grain as well as the He pit volume.

a uniform zircon density of 4.6 g cm^{-3}. Parent isotope concentrations of ^{238}U, ^{232}Th, and ^{147}Sm are similarly converted into atomic abundances. ^{235}U, while also measured, is computed from ^{238}U using the present-day natural abundance ratio (^{238}U/^{235}U = 137.818; Hiess et al., 2012). The (U-Th-Sm)/He age is then determined using the standard radioactive production equation:

$$^{4}\mathrm{He} = 8\,^{238}\mathrm{U}\left(\mathrm{e}^{\lambda_{238}t}-1\right) + 7\,^{235}\mathrm{U}\left(\mathrm{e}^{\lambda_{235}t}-1\right) + 6\,^{232}\mathrm{Th}\left(\mathrm{e}^{\lambda_{232}t}-1\right) + {}^{147}\mathrm{Sm}\left(\mathrm{e}^{\lambda_{147}t}-1\right) \quad (4)$$

Because time t cannot be isolated on one side of the age equation, the age is calculated iteratively using a Newton-Raphson root-finding algorithm. Age uncertainties are propagated using standard first-order Gaussian error propagation, derived from a Taylor expansion of the age equation about the calculated age and measured inputs.

In addition to determining LA-(U-Th)/He ages, the same LA-ICP-MS spot that provides the parent-element concentrations for the (U-Th)/He calculations also allows simultaneous determination of depth-profile U/Pb ages from by measuring Pb isotopes (^{206}Pb, ^{207}Pb, ^{208}Pb). This represents a significant bonus and advantages over conventional dissolution-based (U-Th)/He dating. U/Pb ages in this study were calculated in the same script used for the parent nuclide concentration reduction, using GJ-1 zircon as the primary standard (Jackson et al., 2004) and the same LOESS drift interpolation applied to the NIST 610 sensitivities (Appendix B5). The U-Pb ages are reported without any common-Pb or discordance corrections.

https://doi.org/10.5194/egusphere-2026-4367
Preprint. Discussion started: 12 August 2026

2.6 Machine-learning dispersion modelling

Across all 811 FCT LA-(U-Th)/He spots reported in this study, each analysis is accompanied by a large number of simultaneously measured parameters and their uncertainties, such as the pit volume and pit geometry, matrix composition, trace element data, inclusion contamination, or the compositional zonation observed in the ICP-MS depth profile. Conventional and laser-ablation (U-Th)/He dating are characterized by significant overdispersion which is often hard to attribute to either analytical or geological factors. Different proposed factors governing dispersion in for LA-(U-Th)/He dating, however, can be evaluated as they differentially impact different observed parameters. The deviation of each LA-(U-Th)/He age from the FCT reference age as a function of the different analytical observations can be used as the target of a supervised machine learning model. We explore a gradient-boosted regression tree model (HistGradientBoostingRegressor (HGB), as implemented in scikit-learn; Pedregosa et al., 2011; Appendix D1) to regress the assigned age residual against 33 different co-measured parameters for each in-situ age. The parent and daughter concentrations themselves (^{4}He, ^{238}U, ^{232}Th) are deliberately excluded from the predictor set, as including them could allow the model to use these primary quantities to compensate and correct the dispersion via the age equation (i.e. associating old age residuals with U-Th deficits or ^{4}He excesses), rather than identify the underlying physical or analytical causes for the age dispersion.

All performance metrics and per-spot age predictions are reported from out-of-fold (OOF) cross-validation. For this purpose, the dataset is split into ten folds, with the model trained on nine and used to predict the tenth, and the full procedure is repeated ten times over different random partitions. The predictive contribution of each parameter is evaluated using permutation importance, which measures the decrease in model performance when a parameter is randomly shuffled, and SHapley Additive exPlanations (SHAP) values (Lundberg and Lee, 2017), which decompose individual predictions into feature-level contributions. Two additional safeguards are applied to distinguish real drivers from false correlations in the dataset. The model is refit on multiple bootstrap subsamples to test how consistently each parameter is identified as important and a null-model baseline is established in which the target residuals are randomly reshuffled prior to fitting. It is important to note here that this analysis establishes correlation, but not direct causation, especially since several predictors are correlated with each other as well. For broader interpretation, the 33 input parameters are grouped into seven categories (Geometry/Ablation, QMS/He signals, ICP-MS Chemistry, Mineralogy Fractions, Zonation, U-Pb Context, and Time/Session), and group-level effects are evaluated using leave-one-group-out (LOGO) model comparisons. The purpose of this analysis is not to retroactively correct individual ages, but to identify which measured variables contain reproducible predictive information about age dispersion, and to evaluate whether those predictors can be linked to known physical or analytical drivers.

3 Results

3.1 Interferometer and CT volume benchmarking

The results of the systematic comparison of our interferometric and μ-CT pit volumes (Fig. 5) show a strong correlation (R^2 = 0.9954) and an insignificant bias (mean bias = -0.48%) over the range of pit sizes commonly used for LA-(U-Th)/He. While this

https://doi.org/10.5194/egusphere-2026-4367
Preprint. Discussion started: 12 August 2026

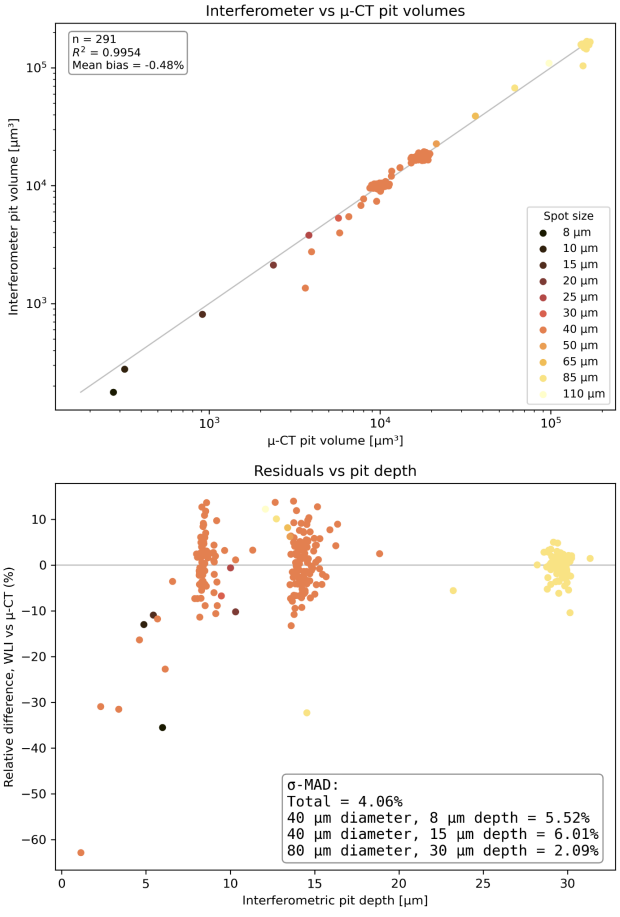

Figure 5. Comparison of µ-CT and interferometer volumes obtained by the two methods in a polished gem-quality zircon.

overall underscores the accuracy of our interferometric pit volume determinations, scatter within the dataset can be significant, and in part depends on the depth and diameter of the ablated pits and the resolution of the µ-CT scan. The σ_{MAD} values (median absolute deviation scaled to 1σ; 1.4826 × MAD) of the relative difference between the two methods for a population of pits of 40 µm diameter / 8 µm depth, scanned at 1.02 µm resolution, and a population of pits of 40 µm diameter / 15 µm depth, scanned at 3.41 µm resolution, is 5.5 – 6%. Larger pits, at 80 µm diameter / 30 µm depth, scanned at 3.41 µm resolution, only show a σ_{MAD} of ∼2%. Ablation spot sizes <15 µm and very shallow pits almost universally show lower interferometric volume values compared to the µ-CT volumes. It is not apparent in our dataset whether this is the result of the low resolution of the µ-CT or a bias in the interferometer measurement itself. These values represent a combined uncertainty and therefore place an upper bound on the interferometer uncertainty.

Overall, the µ-CT data support the accuracy and negligible bias of our interferometric method. Nonetheless, the µ-CT comparison suggests that the precision of individual pit measurements in real applications is only secondarily controlled by point-

https://doi.org/10.5194/egusphere-2026-4367
Preprint. Discussion started: 12 August 2026

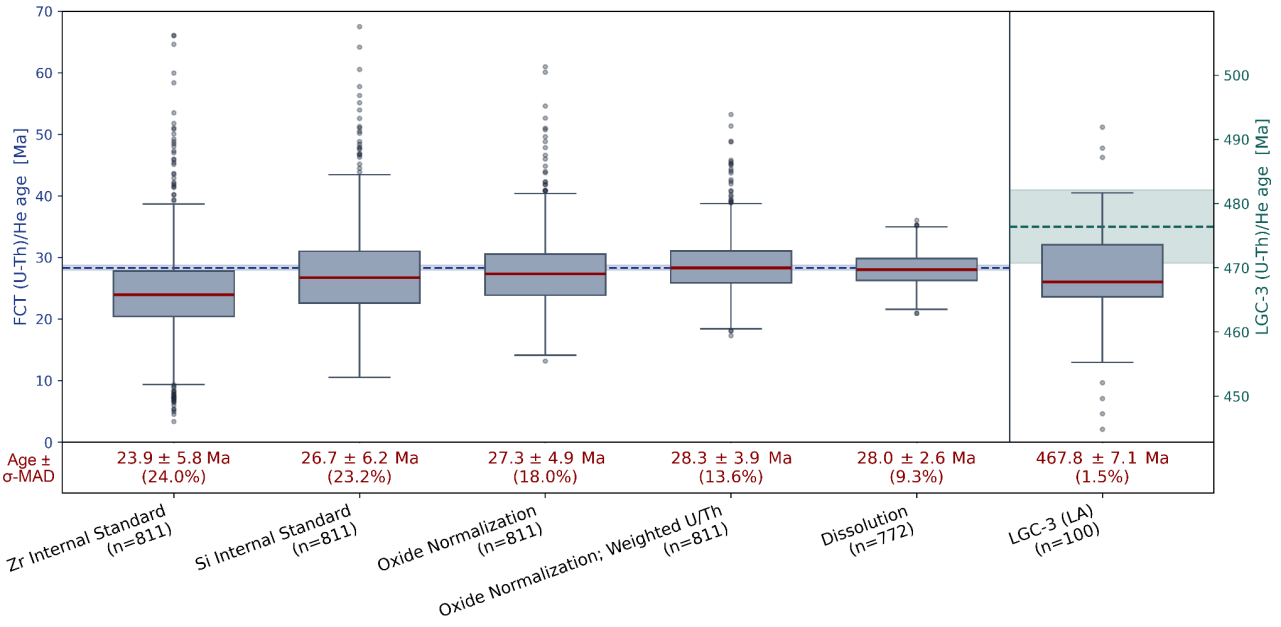

Figure 6. Compilation of LA-(U-Th)/He ages of 811 spots in Fish Canyon Tuff zircons, compared to the conventional dissolution method. An additional 100 spots were measured in the gem-quality mineral standard LGC-3 and reduced using the oxide normalization method combined with parent weighting.

cloud noise, while pit-size and geometry-related effects dominate. In that context, our adoption of a 2% global systematic uncertainty is a reasonable choice for the interferometric method itself, as this value is consistent with the scaled residual scatter of our best-constrained µ-CT dataset. At the same time, our dataset also suggests an increase of this "base" scatter towards smaller and shallow pits, and potentially even an inability to measure pits below a certain size.

3.2 (U-Th)/He age distributions

LA-(U-Th)/He age distributions obtained with each of the four reduction methods described in Sect. 2.5 are presented in Fig. 6, alongside the compiled multi-year conventional FCT whole-grain dissolution dataset (n=772) and the LGC-3 laser-ablation dataset (n=100). We report the median and a σ-normalized median absolute deviation (σ_{MAD}) for each group.

The precision of the FCT data between the four LA reduction methods improves systematically with each methodological refinement. Simply using either ^{29}Si or ^{91}Zr as the internal standard yield medians of 26.7 ± 6.2 Ma (23.2%) and 23.9 ± 5.8 Ma (24.0%), respectively. Reducing the concentrations by stoichiometric oxide normalization tightens the distribution to 27.3 ± 4.9 Ma (18.0%) and brings the median within ∼1 Ma of the independent reference age. Incorporating parent-source depth weighting into the oxide-normalized concentrations produces the closest agreement of any of our four refined approaches with an age of 28.3 ± 3.9 Ma (13.6%), matching the reference within uncertainty and reducing the overall dispersion by a factor of ∼1.7 relative to the ^{29}Si/^{91}Zr-based parent nuclide concentration determinations. The improvements in the FCT age

https://doi.org/10.5194/egusphere-2026-4367
Preprint. Discussion started: 12 August 2026

dispersion across these four reduction schemes directly reflect the effects of minimizing known sources of analytical bias. The internal standard approaches are the most sensitive to spot-to-spot matrix variation, because the assumption of a constant element/internal-standard ratio breaks down in the presence of mineral inclusions or non-stoichiometric ablation volumes. This seems to be especially relevant for the use of ^{91}Zr, which can introduce a significant error when drilling through Zr-free mineral inclusions (Fig. 3) and is clearly evident in our dataset as a broad tail of low apparent ages. The median age of the ^{91}Zr-based dataset is also noticeably lower, likely the result of a combination of two effects: (1) Zr in zircons is commonly substituted by Hf up to a few wt%, violating stoichiometric assumptions and (2) Zr concentrations in NIST are orders of magnitude lower than the stoichiometric concentration in a zircon (448 ppm vs. ∼15.3 wt%). Extrapolating concentrations over several orders of magnitudes likely result in systematic deviations from linear extrapolations in ICP-MS data (Shaulis et al., 2010), potentially leading to systematically higher concentration values.

The additional step of parent-source depth weighting further addresses the geometric mismatch between the distribution of parent elements and the simple averaging of the entire ablated ICP-MS volume. The magnitude of the improvement from this step (σ_{MAD} from 18.0% to 13.6%) indicates that parent-depth bias can account for a substantial fraction of the residual dispersion in simply averaged LA-(U-Th)/He datasets.

We compared 772 single-grain dissolution FCT ages acquired over several years at UTChron Laboratory to provide a reference for the dispersion achievable by conventional (U-Th)/He analysis of the same material (Fig. 6). The dissolution median of 28.0 ± 2.6 Ma (9.3%) agrees with the oxide-normalized, depth-weighted LA-(U-Th)/He age within uncertainty. Its σ_{MAD} value, however, is ∼1.5× smaller than the best-case LA dispersion. Even after correcting for the largest identifiable analytical biases, the FCT dispersion cannot simply be explained by propagated analytical uncertainty alone, which mostly ranges between 2–5 % for the FCT LA analyses. The LGC-3 LA dataset provides an important comparison: its median of 467.8 ± 7.1 Ma corresponds to a σ_{MAD} of only 1.5% (Fig. 6), demonstrating that the workflow can produce substantially tighter age distributions on inclusion-free, unzoned grains. We therefore interpret the larger FCT dispersion as reflecting FCT-specific sample, geometric, or spot-scale effects, rather than the irreducible precision limit of the analytical workflow itself.

3.3 Trace elements, zonation, and U-Pb ages

Accompanying the U-Th measurements, the LA-ICP-MS spot on each grain provides a parallel trace-element, zonation, and U/Pb dataset (Fig. 7). Median ^{238}U and ^{232}Th concentrations are 379.3 ± 197.5 ppm (52.1%) and 247.6 ± 108.7 ppm (43.9%), respectively, with ^{4}He concentrations of 72.0 ± 33.6 nmol g^{-1} (46.7%). The large spread in parent-element concentrations is typical for FCT zircons and reflects well-documented grain-scale heterogeneity in zircon populations (Dobson et al., 2008). Depth-resolved profiling through each LA-ICP-MS spot also allows direct quantification of zonation on both magnitude and erraticness (Sect. 2.5.2). Using thresholds of magnitude >2 and erraticness >1.1, respectively, the majority of FCT spots can be classified as “zoned” in U (73%) and Th (83%), while 37% of U profiles and 46% of Th profiles show “erratic” zonation patterns. The asymmetry between the two metrics implies that while most grains are at least somewhat zoned, they often show gradual gradients or few discrete zones with different composition. Ca-zonation is much less common (35% zoned, 32%

https://doi.org/10.5194/egusphere-2026-4367
Preprint. Discussion started: 12 August 2026

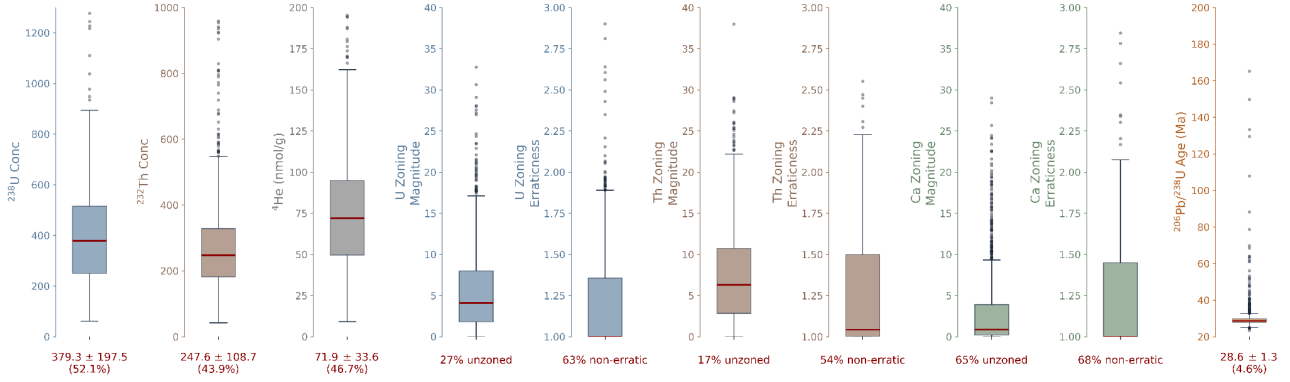

Figure 7. Compilation of U/Th/He concentrations, zonation metrics, and U-Pb ages co-measured on the 811 spots in Fish Canyon Tuff zircons.

erratic). While Ca-zonation can be used as a first-order proxy for apatite inclusions, it can also reflect other Ca-bearing phases, or simply Ca zonation in zircon itself. About 10% of spots exhibit an apatite phase percentage of >1%.

$^{206}Pb/^{238}U$ ages are also reported for each FCT analysis. The ages presented here are not corrected for common Pb and mainly serve as a diagnostic signal rather than an accurate age of grain formation. 91% of the 811 spots yield uncorrected $^{206}Pb/^{238}U$ ages in the expected range of 25–35 Ma (median 28.65 Ma), consistent with the accepted age for Fish Canyon Tuff. However, a small but significant population (5.3%, 43 spots) yielded $^{206}Pb/^{238}U$ ages older than 40 Ma, with seven spots in excess of 1 Ga and up to 1467 Ma. Rather than indicating the presence of older xenocrystic cores, the bulk of these old apparent ages likely reflect the incorporation of common Pb. Measured ^{208}Pb concentrations are systematically higher for these spots, with medians of 3.2 ppm for the >40 Ma population and 7.0 ppm for the >100 Ma population, compared to a dataset-wide median of 0.7 ppm. Because ^{208}Pb includes both common Pb and radiogenic Pb produced from ^{232}Th, these values do not directly quantify common-Pb contamination. Nonetheless, these outliers correlate with the presence of mineral inclusions in the ICP-MS depth profile, particularly feldspar and other aluminosilicates, which are plausible carriers of common Pb without a significant U contribution. A small number of spots may still reflect genuine xenocrystic inherited cores, but these appear to be rare.

3.4 Machine-learning dispersion model performance and feature importances

Across ten repeated cross-validation runs, the HGB model recovers a robust signal from the FCT residuals: out-of-fold (OOF) variance explained is 28.7 ± 1.7%, with an unexplained σ_{MAD} of 3.05 Ma, equivalent to a reduction of 21% from the observed (i.e. the spread in our measured dataset) σ_{MAD} of 3.85 Ma (Table 1). OOF variance explained is dimensionless: it is the fraction of the observed residual variance that the model predicts for spots it has never seen during training, where 100% would be perfect prediction and 0% no better than always predicting the mean. For noisy single-spot geochronological data, ∼29 % therefore constitutes a strong signal. The null-model comparison confirms this, as a parallel run with shuffled targets produces

https://doi.org/10.5194/egusphere-2026-4367
Preprint. Discussion started: 12 August 2026

Table 1. Performance metrics of the HistGradientBoosting regression model trained on the 33 per-spot parameters, evaluated by 10-fold cross-validation repeated 10 times.

Metric	Real targets	Shuffled (null)
Scaled MAD observed (Ma)	3.85	
OOF explained variance (%)	28.7 ± 1.7	-26.8 ± 2.9
Scaled MAD unexplained (Ma)	3.05 ± 0.05	4.48 ± 0.11
Mean absolute error (Ma)	2.70 ± 0.03	3.79 ± 0.05

an OOF variance explained of $-26.8 \pm 2.9\%$ (i.e. worse than the mean) and zero features passing the joint stability threshold, demonstrating that the importances reported here reflect genuine structures in the dataset rather than random correlations or an overfitting of the model.

The OOF unexplained residuals retain a σ_{MAD} of 10.8% of the FCT eruption age, down from 13.6% in the measured dataset. The model therefore captures a measurable and potentially mechanistically interpretable component of the FCT dispersion, corresponding to roughly one third of the observed total uncertainty. The remaining dispersion is not predicted by the measured spot-scale parameters used here, indicating either that important controls are unmeasured, that relevant information is present only in more complex three-dimensional form, or that some scatter reflects stochastic analytical or sample-specific effects not captured by the current feature set. A high-level summary of the per-spot contribution of each feature to the model's predictions is shown as a SHAP beeswarm plot in Fig. 8.

At the group level (Table 2), the LOGO analysis reveals that this reduction is largely due to a small number of parameters. Removing the Geometry/ablation group increases the unexplained σ_{MAD} by +0.37 Ma, which is by far the largest impact of any group. The ICP-MS chemistry group is the second-largest contributor (+0.18 Ma), followed by the U–Pb context group, which carries substantial individual permutation importance (+0.088 ΔR^2) but redundant LOGO behavior, as discussed below. Removing the Zonation group changes the σ_{MAD} by only +0.003 Ma, and removing the Mineralogy fractions group by +0.04 Ma, which for both groups is within or near the noise of the cross-validation. The Time/session and QMS/He signal groups carry essentially no unique information beyond what is already embedded in pit volume. Their LOGO removal only slightly improves OOF performance (-0.11 and -0.03 Ma, respectively), consistent with mild redundancy.

The He pit volume (µm^3) is the single most important predictor across every diagnostic in Table 2. Its permutation importance of 0.343 is an order of magnitude larger than the next-ranked feature, and it achieves a bootstrap stability of 1.00, i.e. it is retained as predictive in all of the 50 bootstrap refits of the model. Its partial dependence (Fig. 9) correlates roughly linearly with the measured pit volume, with the predicted residual decreasing from approximately +5 Ma at the smallest measured volumes ($\sim$2000 µm^3) to approximately -3 Ma at the largest ($\sim$3400 µm^3), with a slope that corresponds to roughly +0.8 Ma in age residual per 10 % reduction in measured volume. After volume, the second-most robust feature in the model is the ^{208}Pb concentration (PI = 0.047, stability 1.00 on both criteria). Its partial dependence (Fig. 9) is steeply decreasing from low

https://doi.org/10.5194/egusphere-2026-4367
Preprint. Discussion started: 12 August 2026

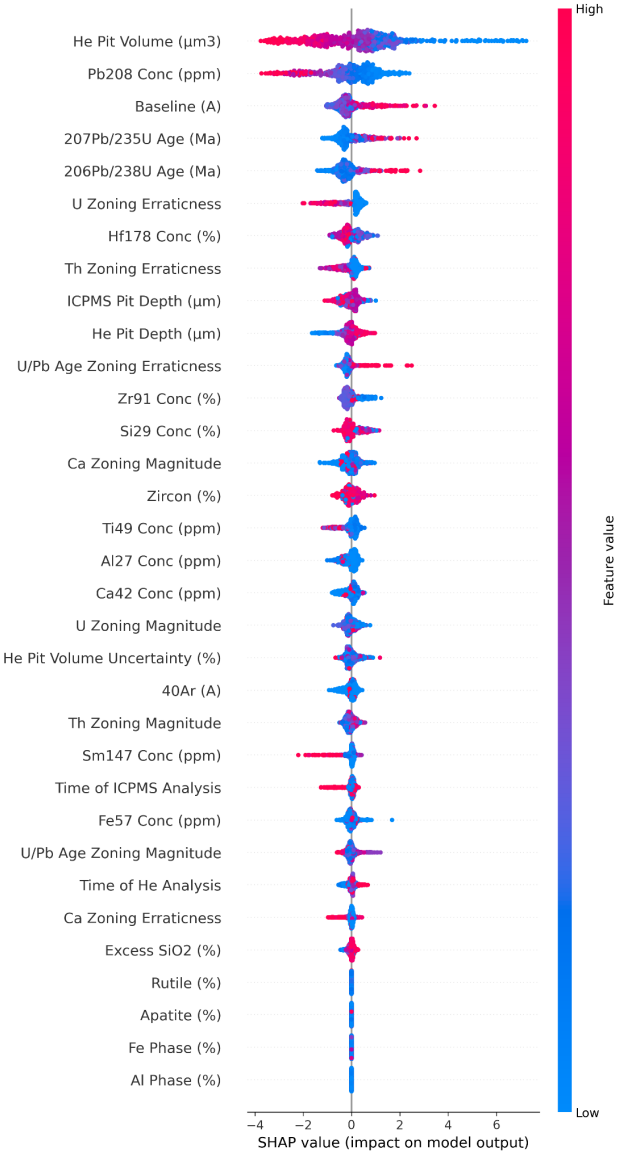

Figure 8. SHAP beeswarm plot summarizing the per-spot feature contributions. Each point corresponds to one spot, colored by its relative value for that feature. The horizontal position of each point indicates the magnitude and direction of that feature's contribution to the model's predicted age residual: positive SHAP values push the prediction toward older apparent ages, negative values toward younger.

^{208}Pb concentrations: spots with the lowest ^{208}Pb have predicted residuals near +2.5 Ma, while spots with ^{208}Pb above ∼1.5 ppm have predicted residuals near −1.5 Ma. A smaller but important signal is carried by the He mass spectrometer Baseline (PI = 0.063, stability 0.96–1.00), whose partial dependence (Fig. 9) is a discrete step function rather than a smooth correlation: spots with baseline below ∼0.144 A have predicted residuals near zero, while spots above ∼0.146 A jump to ∼+1.6 Ma. Sm

https://doi.org/10.5194/egusphere-2026-4367
Preprint. Discussion started: 12 August 2026

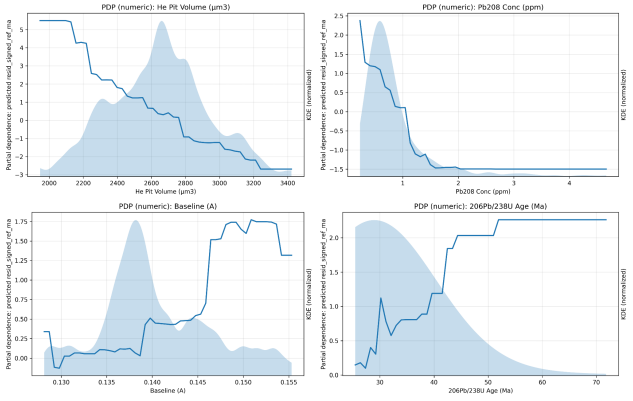

Figure 9. Partial dependence plots (PDPs) for the four strongest predictors in the gradient-boosted regression model. PDPs show the model-predicted effect of one predictor on the target variable while averaging over the observed distribution of all other predictors. Here, the target variable is the signed age residual relative to the FCT reference age in Ma. Positive values indicate predictions toward older apparent ages, whereas negative values indicate predictions toward younger apparent ages. KDE plots in the background show the distribution of feature values.

concentration shows high stability (0.88–1.00 on both criteria), but near-zero permutation importance. None of the individual zonation features achieves a permutation importance above 0.023, and four of the six Mineralogy fractions features (Rutile %, Apatite %, Al Phase %, Fe Phase %) have permutation importance and bootstrap stability of exactly zero, as the model never finds a use for these phase fractions across the 50 bootstrap fits.

4 Discussion

4.1 Pit-volume-correlated effects

As He concentrations are calculated from the ratios of measured ^{4}He to ablated volume, an underestimate of pit volume will directly result in an overestimation of ^{4}He and therefore an older apparent age of the same magnitude. The sign of the partial-dependence relationship (Fig. 9) is therefore consistent with volume error contributing to the age residuals. However, the ML result alone cannot distinguish true interferometric volume-measurement error from other effects that might influence pit volumes, such as ablation efficiency, pit morphology, surface roughness or tilt, inclusion-related ablation behavior, focusing differences, or session-specific operating conditions. We therefore interpret He pit volume simply as the strongest volume-correlated predictor of residual age bias, and not necessarily as a unique proof that interferometeric measurement error is the sole culprit. A potential concern, however, is that He pit volume is highly correlated with several non-geometric variables, most notably Time of He Analysis (r_s = −0.76), the ^{40}Ar signal during He analysis (r_s = +0.68), and Time of ICP-MS Analysis (r_s = −0.53). Based on this correlation, one could argue that pit volume is acting as a hidden proxy for an unrelated temporal or instrumental drift. Ablated volumes could, for example, decrease over the course of the session, as the laser

https://doi.org/10.5194/egusphere-2026-4367
Preprint. Discussion started: 12 August 2026

Table 2. Group-level decomposition of the HistGradientBoosting model, showing the two most important features of each group. LOGO $\Delta\sigma_{\mathrm{MAD}}$ (Ma) is the increase in unexplained out-of-fold scatter when the entire group is removed from the model: larger values indicate that the group carries more unique predictive information. Permutation importance, PI (ΔR^2), is the decrease in OOF variance explained when a feature is individually shuffled, i.e. the share of the model's predictive power attributable to that feature. Mean |SHAP| (Ma) is the absolute per-spot contribution of the feature to the predicted age residual, averaged over all spots and expressed in the same units as the residuals. The full results can be found in Appendix D2.

Group or feature	**LOGO $\Delta\sigma_{\mathrm{MAD}}$ (Ma)**	**PI (ΔR^2)**	**Mean |SHAP| (Ma)**
Geometry / ablation	+0.371	+0.337	–
He pit volume (μm^3)	–	+0.343 ± 0.061	1.445
He pit depth (μm)	–	+0.009 ± 0.011	0.273
ICP-MS chemistry	+0.181	+0.050	–
^{208}Pb concentration (ppm)	–	+0.047 ± 0.023	0.769
^{178}Hf concentration (%)	–	+0.009 ± 0.010	0.221
Mineralogy fractions	+0.039	−0.008	–
Zonation	+0.003	+0.046	–
Ca zoning magnitude	–	+0.022 ± 0.011	0.180
Th zoning erraticness	–	+0.016 ± 0.009	0.259
QMS / He signals	−0.034	+0.065	–
Baseline (A)	–	+0.063 ± 0.033	0.466
^{40}Ar (A)	–	+0.001 ± 0.007	0.203
U–Pb context	−0.098	+0.088	–
^{206}Pb/^{238}U age (Ma)	–	+0.072 ± 0.014	0.381
^{207}Pb/^{235}U age (Ma)	–	+0.018 ± 0.010	0.401
Time / session	−0.106	+0.015	–

energy naturally decreases with time. Consequently, this could correlate with, without any causation, a decrease in ages with time due to an independent effect (such as an insufficiently corrected machine drift). However, two lines of evidence make a purely temporal-drift explanation unlikely. (1) When the temporal and instrumental variables are evaluated separately, their permutation importances are much smaller than the volume signal. (2) the LOGO analysis shows that removing the entire Time/Session group does not degrade OOF performance, indicating that the residual signal carried by these variables is largely redundant with pit volume and other predictors.

As shown earlier in Sect. 3.1, a comparison of interferometer to micro-CT volumes on the same set of pits shows agreement of the median to within ∼1% over the large range of volumes measured, but with a 1σ scatter of 2–6% on individual pits. The ML results add an important distinction to this result, showing that even if interferometer volumes are unbiased on average, individual volume-correlated errors or pit-geometry effects can still contribute measurably to age dispersion. Interestingly, the

https://doi.org/10.5194/egusphere-2026-4367
Preprint. Discussion started: 12 August 2026

pit volume uncertainty (in %) does not correlate with dispersion, which one would expect in the case that "bad" pits (e.g., "popcorn", irregularly shaped pit walls and bottoms, etc.) cause less precise volume measurements. The much better precision of the LGC-3 dataset, measured on a grid of 10 × 10 spots on a polished surface of a gem-quality zircon, indicates instead that much of this dispersion is the result of grain-to-grain variations. Plausible causes of this variation include slightly tilted or rough surfaces, the presence of inclusions with different ablation characteristics, or small changes in how well the laser is focused between spots.

Among the measured predictors, He pit volume is both the strongest and one of the most experimentally tractable. The µ-CT comparison and the ML model therefore both imply that improving the precision, reproducibility, and calibration of individual pit-volume measurements directly improve age accuracy and reduce LA-(U-Th)/He dispersion. This highlights the need for further work on grain-to-grain ablation behavior, pit-shape reproducibility, interferometric volume calibration, and the development of suitable volume standards.

4.2 Inclusions, common Pb, and apatite proxies

Within the ML model, elevated ^{208}Pb is the strongest chemical predictor of age residuals, with high 208Pb concentrations correlating with younger ages. ^{208}Pb also correlates with Al-based inclusion proxies (r_s = +0.44) and the Fe-bearing phase fraction (r_s = +0.35) and anticorrelates with the zircon fraction (r_s = −0.42) High-^{208}Pb spots therefore robustly identify ablated volumes that intersect non-zircon mineral inclusions. As the measured ^{208}Pb is a mixture of the common lead component and radiogenic ^{208}Pb produced from ^{232}Th, it is not a unique proxy for common-lead carrying aluminosilicate inclusions but also Th-bearing phases such as apatite. We therefore interpret its association with younger (U-Th)/He age residuals as a general signal of inclusion-related disturbance. As our dataset can only establish correlations, the exact cause for the correlation with younger ages remains speculative, although plausibly inclusion-host interfaces could facilitate He loss through microcracking or enhanced diffusion. Interestingly, the uncorrected ^{206}Pb/^{238}U age shows the opposite relationship, with older apparent U-Pb ages associated with positive (U-Th)/He residuals. These ages may therefore reflect common-Pb-bearing inclusions or rare inherited zircon domains, but the dataset does not distinguish between these possibilities. The two Pb-related predictors should therefore not be treated as equivalent measures of common-Pb contamination.

Sm concentration and the modeled apatite fraction carry little independent predictive information. The measured apatite proxies provide no clear evidence that apatite inclusions systematically bias the ages, although their effects may partly overlap with the broader ^{208}Pb inclusion signal.

4.3 Zonation and the limits of the 1D U-Th characterization

The perhaps most unexpected result of the ML analysis is the negligible contribution of the zonation group. Despite the inclusion of six features that quantify the magnitude and erraticness of U, Th, and Ca zonation along the depth-resolved ICP-MS profile, the group's removal increases the OOF σ_{MAD} by only 0.003 Ma, within the noise of the cross-validation. These results are not automatically evidence that zonation in general is unimportant in (U-Th)/He systematics. It is well established that zonation is among the principal sources of dispersion in conventional dissolution datasets (Hourigan et al., 2005; Dobson

https://doi.org/10.5194/egusphere-2026-4367
Preprint. Discussion started: 12 August 2026

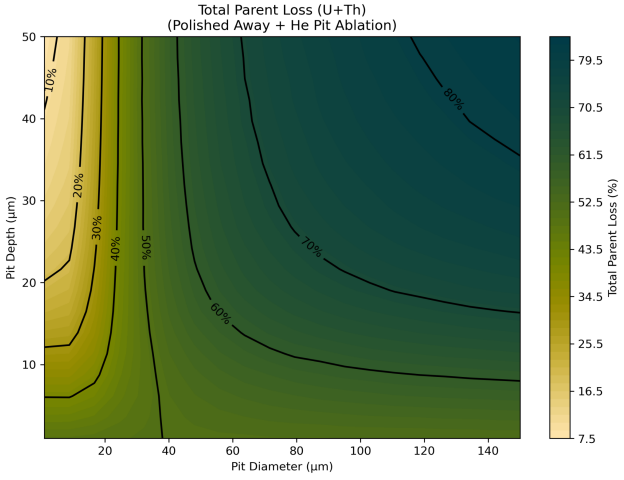

Figure 10. Modeled fraction of U+Th parent-source locations that are unavailable to the subsequent ICP-MS measurement because they were either removed during polishing or consumed during He-pit ablation. Parent loss depends strongly on pit geometry: narrow, deeper pits reduce the contribution from the polished-away surface region, whereas larger-diameter pits remove a larger fraction of the parent-source volume.

et al., 2008). We interpret the absence of a predictive signal to instead be the result of the effect of the data-reduction workflow: Oxide normalization reduces matrix-composition bias, and parent-source depth weighting reduces the bias associated with vertical parent-element gradients sampled by the ICP-MS profile. After these corrections, the measured U, Th, and Ca zonation metrics add little independent predictive information about the remaining age residuals. It is important to note that this does not mean that all zonation-related effects have been removed. Within-spot zonation does exist beyond what we can measure, as within-spot zonation metrics are by construction a 1D characterization of a 3D phenomenon. LA-ICP-MS is intrinsically a method with a very high depth resolution, but very low lateral resolution. Our depth profile is essentially blind to any lateral variation in U and Th concentrations and instead averages the signal for each time step from an analyzed cylindrical volume that is only ∼0.2 µm deep, but ∼60 µm wide. If the grain is laterally zoned at sub-stopping-distance scales, this internal alpha redistribution introduces a mismatch between the U-Th measured at the spot and the U-Th sources of the He measured. More importantly, the portion of the grain removed during polishing and the ablation of the He pit (Fig. 10) is itself not recoverable in our zonation metric. The same logic applies to the modal mineralogy fractions. A spot's nominal "apatite %" for example reflects only the mineral makeup of the ablated cylinder, whereas inclusions that disturb the He budget of the surrounding zircon often extend far outside the sampled ICP-MS volume. Consequently, any residual dispersion attributable to zonation is most likely to involve U-Th heterogeneity that is not captured by the measured one-dimensional ICP-MS profile, either because it occurs laterally within the preserved grain volume or because it was located in material removed prior to ICP-MS analysis.

https://doi.org/10.5194/egusphere-2026-4367
Preprint. Discussion started: 12 August 2026

4.4 The "ghost grain" volume as the primary driver of dispersion

To estimate the magnitude of the eU bias introduced by extrapolating our 1D ICP-MS profile to a 3D parent-source distribution, we constructed a simple "layered-cake" zonation model in which the zircon is divided into two laterally homogeneous layers of different eU concentration separated by a horizontal boundary at depth relative to the polished surface. For each boundary position we compare three eU calculation methods: a simple unweighted average over the 0–25 µm ICP-MS profile, the parent-source-weighted estimate over the same depth window, and a parent-source-weighted full-profile reference that extends into the polished-away rim and the surrounding bulk, representing the unbiased eU that no measurement of the polished grain can recover. Real zircons exhibit more complex 3D zonation patterns, so the results should be read as a simplified error envelope to investigate the mismatch introduced when part of the parent-source region lies in material that was removed before ICP-MS analysis.

For rim-enriched grains with He and ICP-MS pit depths similar to the ones used for the data in this study, the simple average and the parent-weighted estimate coincide and both systematically underestimate eU, with errors approaching -80% when the layer boundary lies near the polished surface (Fig. 11a). The two methods result in the same error because no information about the original high-eU rim survives polishing, and depth weighting cannot recover material that is no longer present. For core-enriched grains, both estimators overestimate eU, but the parent-weighted estimator caps at +55% while the simple average reaches +160%. The parent-source depth weighting cuts the maximum systematic error by a factor of $\sim$3 but cannot eliminate it. Increasing the He pit depth from 5 to 15 µm further reduces the maximum error (Fig. 11b). At a contrast factor of 10, the error for core-enriched grains decreases from approximately 60% to 30%. A deeper He pit shifts the He-budget-relevant volume downward into the preserved part of the grain, thereby reducing the contribution of the polished-away rim to the true eU.

These modeled errors are more than sufficient to generate offsets of the magnitude of the entire residual dispersion. Across our 811 FCT spots, the median U zonation magnitude metric is 4.1. At a contrast of $\sim$4, the layered-cake model predicts maximum eU errors of approximately -60% for rim-enriched and +40% for core-enriched configurations under the parent-source-weighted reduction (Fig. 11b, 5 µm pit). Propagated through the (U-Th)/He age equation on a 28 Ma grain, these worst-case eU biases correspond to age residuals of approximately +40 Ma and -8 Ma and therefore well in excess of the unexplained σ_{MAD} of $\sim$3 Ma that remains after ML correction, even allowing for the fact that most grains will not sit at the worst-case geometry. The comparison between our two samples provides an independent test of this interpretation. The LGC megacryst was measured with the exact same analytical workflow as the FCT zircons yet yields a σ_{MAD} of only 1.5 %. Because LGC is compositionally homogeneous, the material removed during polishing is identical to the material measured, meaning there is no bias from the polished-away volume contribution. The residual dispersion of LA-(U-Th)/He ages is therefore not set by the precision of the analytical workflow, but by zonation "hiding" in the polished-away section of the grain, which no refinement of the current LA-(U-Th)/He workflow can solve. Additionally, our simplified two-layer model only predicts maximum possible offsets rather than the errors from more complex three-dimensional zonation within the preserved grain,

https://doi.org/10.5194/egusphere-2026-4367
Preprint. Discussion started: 12 August 2026

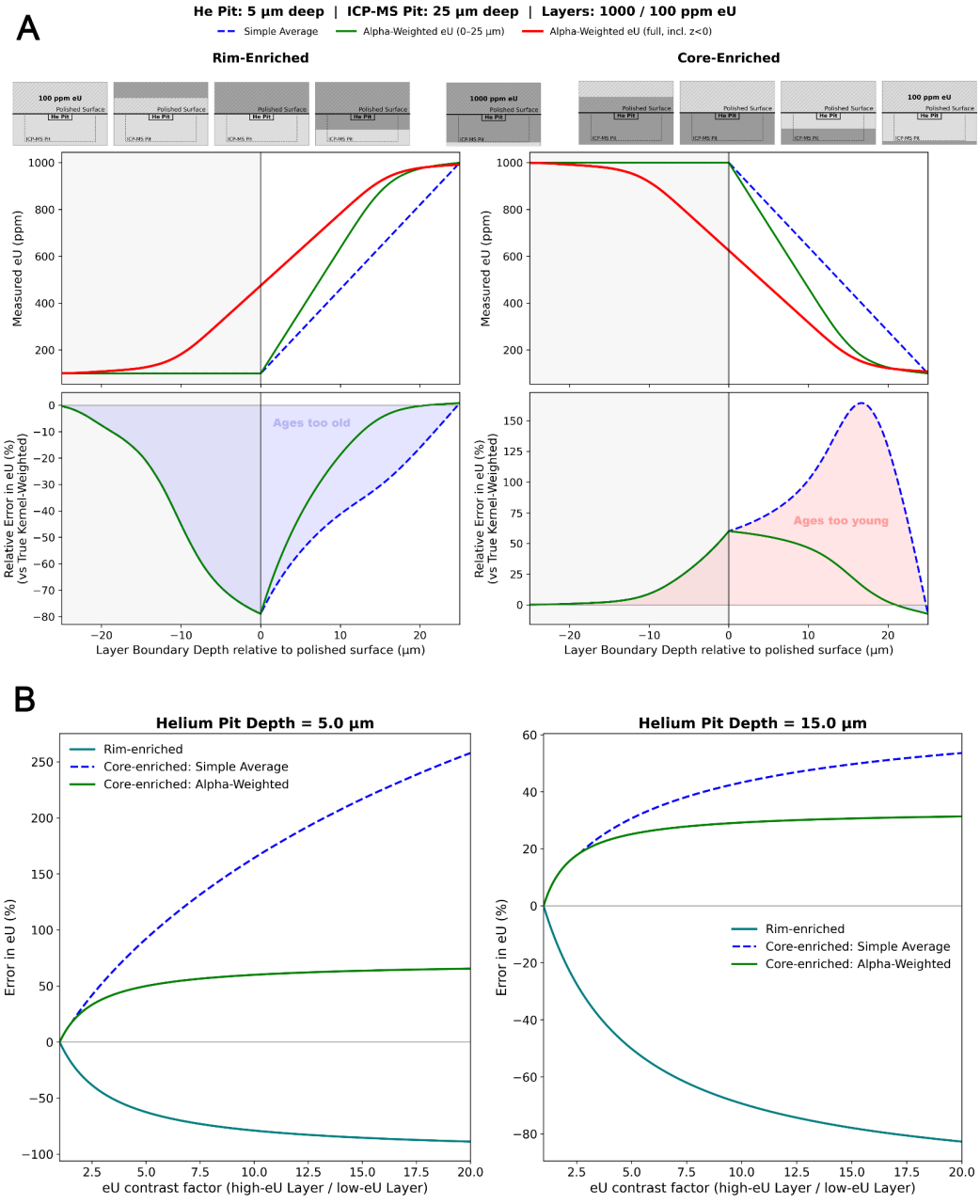

Figure 11. Simplified layered-cake model illustrating eU bias caused by parent-element zoning in material removed before ICP-MS analysis. a) For a 5 µm-deep He pit and 25 µm-deep ICP-MS pit, rim-enriched and core-enriched two-layer profiles produce opposite age biases. Parent-source depth weighting reduces the core-enriched bias relative to a simple average but cannot eliminate the error. b) Maximum eU error as a function of eU contrast factor for 5 and 15 µm He pits, showing that deeper He pits reduce the bias by shifting more of the He-relevant parent-source volume into the preserved grain.

https://doi.org/10.5194/egusphere-2026-4367
Preprint. Discussion started: 12 August 2026

which may contribute an even larger error. Constraining that contribution would, however, require direct 3-D parent-element imaging or statistical models of zircon zoning patterns, which is beyond the scope of this study.

The practical implication of our results is that, beyond reducing the volume-correlated uncertainty identified in our ML model, the dispersion of LA-(U-Th)/He ages on zoned grains cannot be substantially improved within the current methodology. Further gains in precision therefore require a method that accounts for the parent-element distribution in the currently polished-away section, for example by characterizing the U-Th zonation of the grain prior to polishing, or by adopting analytical geometries that minimize the He contribution from removed material. Deeper, narrower He pits (Figs. 10 and 11B) represent an immediately testable step in this direction, provided that He yields remain above instrumental detection limits and that pit volumes can still be measured accurately.

5 Conclusions

This study establishes a complete and reproducible workflow for laser-ablation zircon (U-Th)/He dating and identifies the principal limitations that currently control its precision. Dynamic multi-phase oxide normalization improves parent-nuclide quantification by avoiding reliance on a single stoichiometric internal standard and by accommodating mixed mineral phases encountered during ablation. Parent-source depth weighting further improves accuracy and precision by accounting for the non-uniform spatial distribution of the U, Th, and Sm atoms that contributed helium to each extraction pit. Together, these refinements produce Fish Canyon Tuff ages consistent with the accepted reference age and reduce dispersion substantially relative to conventional Si- or Zr-normalized reductions. The dispersion remaining cannot be attributed to an inherent instrumental precision limit. The much less dispersed LGC-3 age distribution demonstrates that the workflow can achieve high internal precision when applied to compositionally homogeneous, inclusion-free material. Nonetheless, the Fish Canyon Tuff results show that age reproducibility depends strongly on interactions among pit geometry, volume determination, inclusions, and parent-element heterogeneity at spatial scales that are incompletely captured by the present measurements.

Our machine-learning analysis provides a quantitative basis for understanding these effects. He-pit volume is the dominant predictor of age residuals, indicating that volume-correlated geometric or analytical effects represent the largest identifiable and potentially correctable source of error. Elevated 208Pb provides an additional practical indicator of potentially disturbed analyses, particularly where inclusions bias the measured parent-daughter relationship. By contrast, measured one-dimensional U-Th zonation and mineral-phase proportions show no statistically significant correlation with age residuals. The absence of this correlation, however, does not imply that zonation is unimportant. The modeling results show that parent-element heterogeneity in material removed during polishing can generate age offsets equal to or larger than the observed residual dispersion. Because this volume is unavailable to subsequent ICP-MS analysis, its composition cannot be reconstructed from the preserved depth profile. Future improvements should therefore focus on calibrated pit-volume standards, more reproducible ablation geometries, systematic screening for inclusion-related disturbance, and extraction strategies using deeper, narrower pits. Ultimately, further gains in precision will require methods that either characterize the complete helium-producing parent-source volume or reduce the contribution of regions destroyed before parent-nuclide measurement.

https://doi.org/10.5194/egusphere-2026-4367
Preprint. Discussion started: 12 August 2026

Appendix A: Methodological setups

A1 PFA mounting and polishing protocol

We tested multiple mounting mediums for our routine. Although indium performs well under UHV conditions, its high cost, opacity, and the inability to polish pressed grains without dislodging them make it impractical for routine use. We also tested Hysol 1C, a UHV epoxy similar to TorrSeal, and found it requires >12 h of baking at ∼120 °C to not degas during analysis. That and its long curing time (up to two days) and opacity make it a less favorable option. PFA Teflon, in contrast, combines all desirable characteristics for LA-(U-Th)/He analysis. To prepare mounts, we developed the following protocol (Fig. 1 of the main text):

(1) An 8 mm disc is punched from a 2 mm thick PFA Teflon sheet.

(2) The disc is fitted into a mask made of a 24 × 46 mm sized Teflon sheet of 2 mm thickness, with an 8 mm hole in its center.

(3) The mask with disk is loaded on a holder and positioned under a WT-QS100 pneumatic hot stamping machine, with the upper plate set to 320 °C. The mount is covered with Kapton film and pressed on both sides for 80 s at a pressure of 0.6 MPa, then weighted down until cooled. This creates an even and smooth surface and removes any warping of the disk.

(4) With the disc remaining inside the mask, the mineral grains to be analyzed can be loaded. Mineral grains placed onto PFA substrates commonly exhibit pronounced electrostatic behavior, including "jumping," lateral movement, or apparent repulsion from tweezers. This behavior reflects the intrinsic properties of fluoropolymers. Since PFA lies at the extreme negative end of the triboelectric series it has a strong tendency to acquire and retain excess electrons (Diaz and Felix-Navarro, 2004). Because both the substrate and the mineral grains are excellent insulators, the accumulated negative charge cannot dissipate and instead generates strong local electric fields. We were not able to eliminate this effect even when using an ESD wrist strap. Moreover, PFA surfaces have very low surface energy and correspondingly low friction, which allows grains to easily slide freely across the surface. These characteristics make precisely positioning mineral grains challenging. To circumvent this issue, we first pipette a small drop of ethanol onto the PFA disk, into which the grains can be transferred using a tweezer. As the ethanol slowly evaporates, the grains can then be rearranged.

(5) Approximately ten Cospheric Soda Lime Solid Glass Microspheres (177.5 ± 2.5 µm) are added to each mount to serve as depth markers.

(6) Once all grains are mounted and properly positioned, the mount is pressed again for 60 s at 0.6 MPa using the upper plate set to 320 °C. The grains are located on the upper surface of the PFA disk and are pressed down during contact with the heated plate through the Kapton film. In contrast to heating the entire disk on a hot plate or in a heated mold, this one-sided, short-duration heating primarily softens the upper PFA surface while limiting bulk heating and deformation of the mount. The mount is then kept under weight until cooled to minimize warping. If air bubbles or cavities remain around individual grains, the pressing step can be repeated.

https://doi.org/10.5194/egusphere-2026-4367
Preprint. Discussion started: 12 August 2026

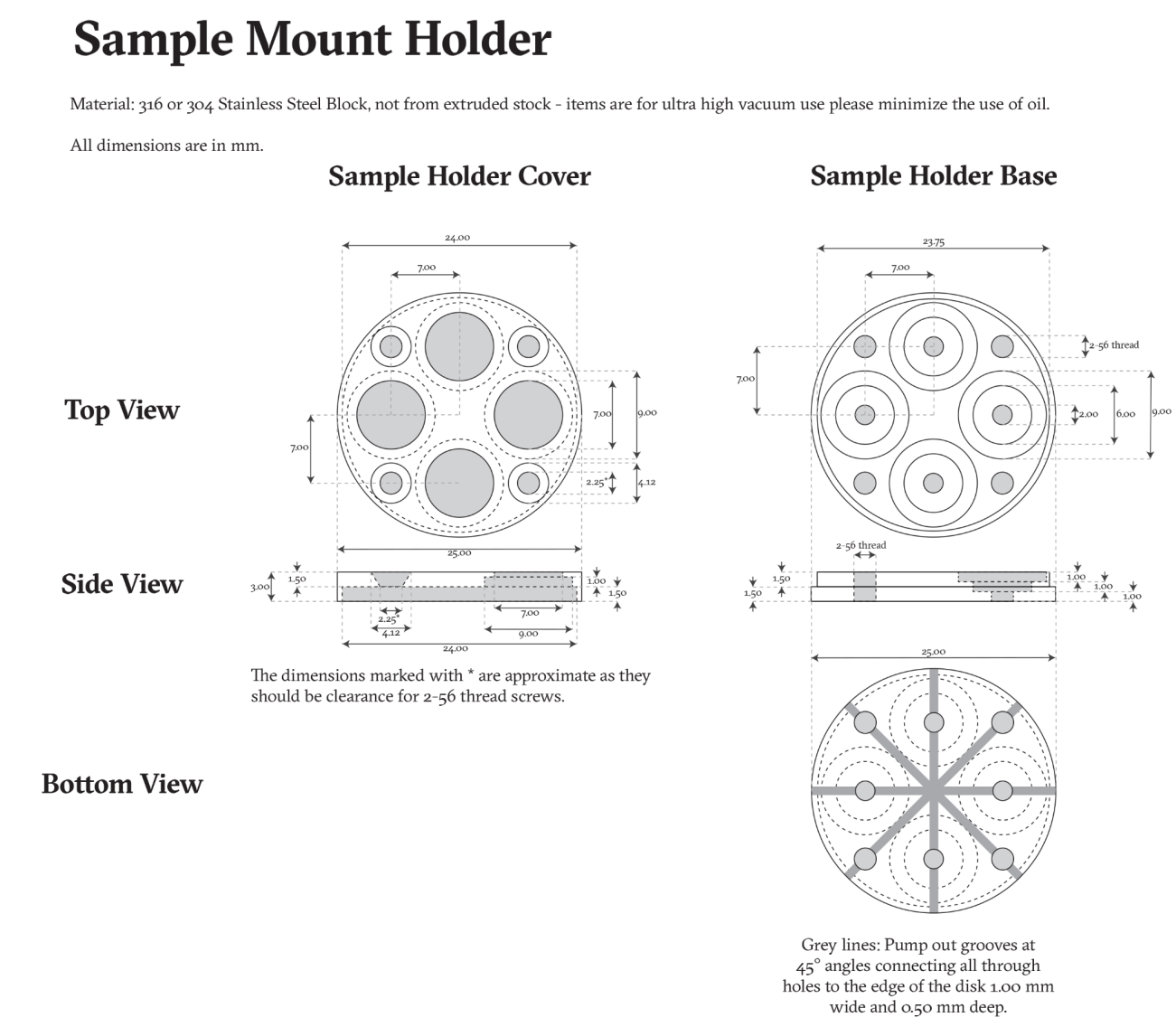

Figure A1. Technical drawings of the custom-designed sample holder

(7) The mounted disc is then removed from the mask and transferred to a custom 3D-printed holder for polishing. Polishing is performed on a Struers RotoPol-22 with a Struers RotoForce-4 automated head. The mount is polished for ∼3 min using a 6 µm diamond suspension, followed by 3 µm and 1 µm suspensions for ∼1 min each.

(8) After polishing, the finished mounts are loaded into the custom-designed sample holder, which accepts up to four PFA mounts and fits both our UHV laser-ablation sample chamber and the ICP-MS sample cell. Technical drawings of the sample holder are provided in Fig. A1.

https://doi.org/10.5194/egusphere-2026-4367
Preprint. Discussion started: 12 August 2026

A2 Laser-ablation system and He extraction line

Laser-ablation under UHV poses some additional challenges. Nano-second pulsed laser ablation systems remove material by depositing energy into the near-surface of a sample faster than the material can thermally respond, leading to rapid electronic excitation, pressure build-up and ultimately phase explosion rather than melting (Russo et al., 2013). Higher laser fluence therefore does not increase melting. When fluence is too low, the deposited energy is insufficient to initiate this transition and instead produces a transient melt layer or incomplete vaporization of sample material, resulting in small melt droplets ("popcorn") in the bottom of the pits (Bleiner and Bogaerts, 2006; Stockli et al., 2017), and large lateral ejecta. These artifacts are especially pronounced under ultra-high vacuum, where plume expansion is ballistic and molten particles can redeposit onto grain surfaces without being swept away by a carrier gas. We have found that the main factors to avoid this issue are regular tuning of laser and optics; ensuring sufficient transmissivity through the sample chamber window; fine-focusing of each analysis spot; ensuring the sample surface is perpendicular to the laser beam and well-polished; and a sufficiently slow repetition rate of the laser to avoid shielding. It is also worth noting that the laser energy is reduced ∼30 % by the optical window (sapphire) of the UHV sample chamber.

Our design of the sample chamber is based on a design by the NG3L laboratory at Arizona State University, and further optimized for a low internal volume, maximizing the laser energy at the sample, and protecting the optical window from ejection residue. Technical drawings of the sample chamber are provided in Fig. A2. The sample chamber consists of three 2.75" diameter ConFlat flanges: (1) A base flange, modified to screw down the sample holder using vented 2-56 screws. (2) A center flange, with an attached 1/4" tube with a 1.33" CF connecting flange at its end. The center flange extends the height of the sample chamber and therefore the distance between sample and window / coverslip. A longer working distance is necessary to significantly reduce or eliminate ejecta from the sample ablation precipitating and covering the optical window, leading to a decrease in the effective laser energy over the course of the analysis (Van Soest et al., 2017). (3) A top flange with a 1.47" diameter DUV-grade sapphire viewport. Sapphire as the material of choice for the optical windows was chosen due to its acceptable transmissivity of ∼65 % for 193 nm UV laser light, while being virtually helium-tight at room temperature. Test runs with an optical window of fused silica, despite its ∼90 % transmissivity for 193 nm UV laser light, were unsuccessful, as helium at room temperature readily diffuses through the material, causing highly elevated blanks. To further minimize the risk of ablation ejecta damaging the viewport, a 38 mm fused silica coverslip is positioned 30 mm above the sample surface and held in place by a tube attached to the base flange. The total internal volume of our sample chamber is ∼30 cm^3.

The sample chamber is attached to the UHV extraction line, which consists of: (1) The sample chamber described above. (2) A Pfeiffer HiCube 80 pumping station, combining a Pfeiffer HiCube 80 Turbomolecular pump with an MVP 015 Diaphragm backing pump, used to pump down the line to UHV after a sample change. (3) A SAES GP50 line getter kept at a temperature of ∼300 °C. (4) A ^{4}He standard tank ("Q-tank") with an initial delivery of 2.95×10^{-13} mol per shot, calibrated manometrically. (5) An ultrapure ^{3}He standard tank with a constant delivery using an automated pipette. (6) A Janis cryogenic charcoal trap. (7) An Agilent 20 VacIon Ion Pump used for routine pumping before and after analysis. (8) A Pfeiffer Vacuum Prisma 200 QMS with a SAES GP50 getter kept at room temperature attached.

https://doi.org/10.5194/egusphere-2026-4367
Preprint. Discussion started: 12 August 2026

During analysis, the line is pumped for 300 s before and after the measurement using the ion pump. After sample ablation and inlet into the extraction line, the released gas (or blank) is mixed with a shot from the standard ^{3}He tank. The gas mixture is then purified on the hot getter for 30 seconds, removing most active gasses. As laser-ablation releases very little gas, the gettering time can be kept to a minimum to reduce the blank. The Janis cryogenic is not used for gas cleanup or cryogenic focusing. After inlet into the QMS, masses 2, 3, 4, 5.5, and 40 are measured in 15 cycles for 0.2 s (masses 2 and 40), and 2 s (masses 3, 4, 5.5) integration time at an SEM amplification voltage of 1000 V. Mass 40 (^{40}Ar) is not used for the ^{4}He calculation, but to monitor the vacuum conditions during the analysis.

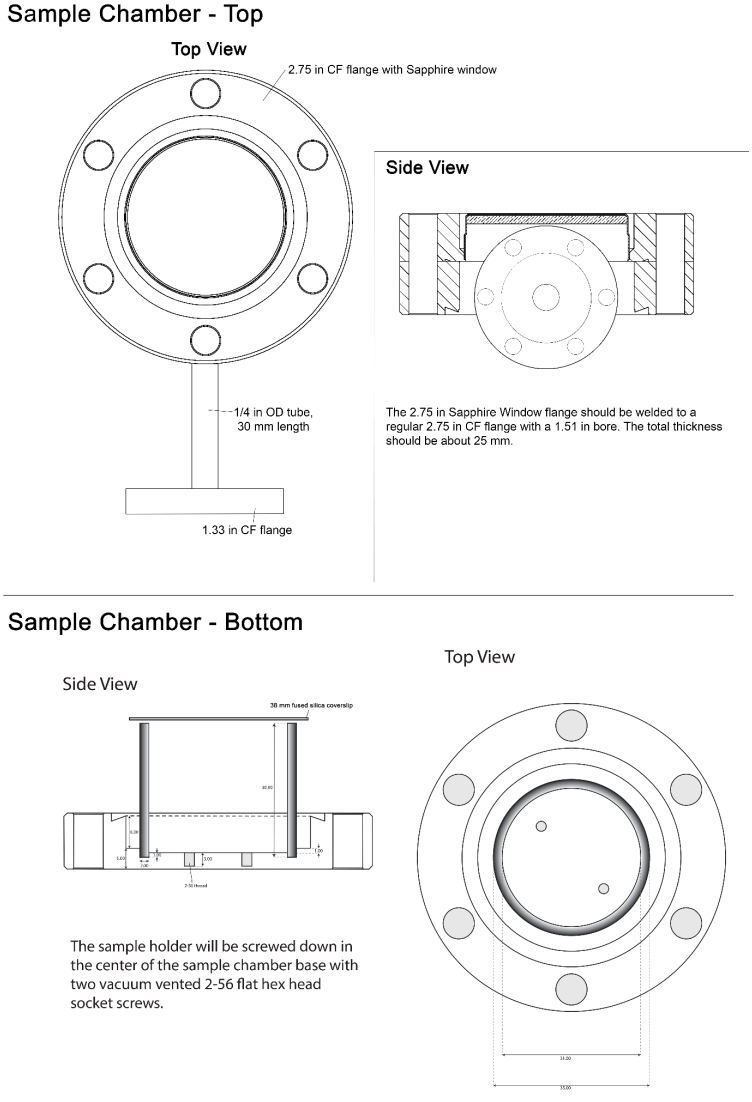

Figure A2. Technical drawings of the custom-designed UHV sample chamber

https://doi.org/10.5194/egusphere-2026-4367
Preprint. Discussion started: 12 August 2026

Appendix B: Data evaluation and reduction

B1 Helium data reduction

For each analysis, the time-resolved signals at masses 2, 3, 4, 5.5, and 40 are regressed linearly against time and extrapolated to their time-zero intercepts. The uncertainty of each intercept is estimated from the standard deviation of the regression residuals.

As the ^{4}He signal is always relative to the signal of the ^{3}He spike, additional corrections are applied prior to the ^{4}He/^{3}He ratio calculations. Measurements at mass 5.5 are used as background measurements for all other masses and subtracted as a dynamic baseline correction. The mass 2 measurement is used to correct for the HD^+/H_3^+ overlap on ^{3}He, assuming a constant $(HD^+ + H_3^+)/H$ ratio of 0.0033. The contribution of these interfering masses on the ^{3}He measurement is <0.5 %. Uncertainties from all corrections are propagated to the final ^{4}He/^{3}He ratio uncertainty. Instrumental blanks, analyzed at regular intervals to bracket sample and standard measurements, are used to correct the measured ^{4}He/^{3}He ratios. All blank and sensitivity corrections are therefore performed in ^{4}He/^{3}He ratio space, which renders the quantification insensitive to drift in the absolute instrument sensitivity. As background levels drift over the course of an analytical session, a global LOESS (Locally Estimated Scatterplot Smoothing) regression is fitted through the blank measurements and utilized to determine the precise blank contribution for a given sample at its exact time of analysis. Because repeated sampling from the finite reservoir of the reference tank predictably reduces its internal pressure, the absolute gas volume of each standard aliquot is corrected for progressive depletion according to:

$$V_n = V_0 \, (Q_{\mathrm{DT}})^n \tag{B1}$$

where V_n is the delivered ^{4}He amount, V_0 is the calibrated initial ^{4}He amount per shot, Q_{DT} is the tank-specific depletion factor (0.99992 for the "Q-tank"), and n is the cumulative shot index (extracted from the analysis metadata). The same depletion correction is applied to the ^{3}He spike tank using its own cumulative shot index. The instrument's sensitivity is then determined by applying an identical LOESS regression used during blank correction to the standard shots. Absolute ^{4}He abundances of each unknown can then simply be calculated by scaling the ^{4}He/^{3}He ratio or absolute signal of unknown and standard.

Uncertainties were propagated through all reduction steps. The uncertainty of each analysis was first taken as the uncertainty of the time-zero intercept from the linear regression of signal versus time, estimated from the standard deviation of the regression residuals. Blank uncertainties were then propagated by Monte Carlo propagation through the LOESS fit (n = 1,000 resamples of the blank measurements within their uncertainties). Final ^{4}He concentration uncertainties were calculated by propagating the uncertainties of the blank-corrected sample signal, the interpolated standard response, and the calibrated standard-gas aliquot, including the depletion correction of the reference tank.

B2 Automated pit-volume determination

Our pit volume extraction code takes the output file from the Bruker interferometer and interpolates a topographic surface from which pit depth, diameter, volume, and their uncertainties are derived:

https://doi.org/10.5194/egusphere-2026-4367
Preprint. Discussion started: 12 August 2026

(1) The Bruker output file (a grid-based .SDF text file) is read in and outlier points within the point cloud removed using a k-nearest-neighbor approach: for each point, the median height of its k = 5 nearest neighbors in the horizontal plane is computed, and points deviating from this local median by more than 5 µm are discarded.

(2) The code then fills the grid by linearly interpolating over missing or bad datapoints, such as from steep pit walls, on a regular grid at the native lateral resolution of the instrument.

(3) A Circle Hough Transform identifies the outline of the pit and extracts the parts of the point cloud containing the pit and surrounding mineral surface. If the automated circle detection fails (e.g. for irregular pit shapes), the pit outline can instead be digitized manually as a polygon.

(4) The mineral surface is separated using a RANSAC-based plane segmentation applied to the upper 70 % of the data points. The entire point cloud is then translated and rotated so that the reference surface lies horizontally at z = 0, removing any tilt in the original mineral surface.

(5) Any points still present above the reference plane are removed to eliminate positive features (most notably ejecta piles at the crater edges). In addition, points shallower than 0.3 µm below the reference plane are discarded to remove residual surface roughness, and isolated points deeper than twice the detected pit-bottom depth are removed as measurement artifacts.

(6) The cleaned point cloud is then downsampled onto a voxel grid at the native point spacing, to homogenize the point density, and interpolated into a continuous triangular surface mesh. A two-dimensional Delaunay triangulation is constructed from the horizontal coordinates of all points, and the measured vertical values are used to generate a watertight three-dimensional mesh.

(7) The total ablated volume is computed by integrating over the triangular mesh. Each triangular facet is treated as the top face of a vertical prism extending down to the reference plane (i.e. the mineral surface). The contribution of each facet to the total volume is obtained analytically from the coordinates of its three vertices. The sum of all prism volumes yields the full pit volume.

(8) The code estimates a pit-specific analytical volume uncertainty by bootstrap resampling of the interferometry point cloud. For each pit, 30 resampled point sets (50 % of points per replicate, drawn with replacement) were propagated through the meshing and integration workflow, and the standard deviation of the resulting volumes, scaled to account for the reduced point density of the subsampled clouds, was taken as the random component of the volume uncertainty. This uncertainty is <1 % for most “clean” spots and only represents the pure analytical uncertainty (i.e. the results of scatter of the interferometer and uncertainties associated with the data reduction scheme). There likely is a significant external uncertainty, owing to the complex pit geometry. Repeated measurements of the same pit at different settings and angles suggest an uncertainty of at least 2 %. This value was therefore added as a global systematic in the quadrature. Final uncertainties are generally 2–5 %.

(9) The pit depth is determined independently using a kernel density estimation (KDE) of the point cloud z-values. The mineral surface is defined as the highest-density peak in a KDE of the plane-inlier points, while the highest-density peak in the surface-corrected pit point cloud (excluding peaks shallower than 10 % of the maximum pit depth) is interpreted to be the main pit bottom. The code also outputs the value of the deepest KDE peak as the maximum pit depth. The pit volume and main pit bottom depth are then used to calculate an equivalent circular diameter, assuming a cylindrical geometry. A significant

https://doi.org/10.5194/egusphere-2026-4367
Preprint. Discussion started: 12 August 2026

deviation of the calculated equivalent circular diameter from the set laser spot diameter can be indicative of a bad pit geometry or a failed volume calculation, e.g. due to "popcorn" filling up most of the pit. In that case, the maximum pit depth, together with the spot radius, can be used to estimate the volume of the unobstructed pit.

B3 Oxide-sum normalization: implementation and uncertainties

For each element i, the instrument sensitivity $S_i(t)$ is determined from repeated analyses of NIST 610 throughout the run:

$$S_i(t) = \frac{\mathrm{CPS}_i^{\mathrm{NIST}}(t)}{C_i^{\mathrm{NIST}}} \tag{B2}$$

where CPS is the background-subtracted net count rate at ablation time t, and C_i^{NIST} is the accepted concentration of element i in NIST 610 (from Jochum et al., 2011). Prior to the sensitivity calculation, all raw signals are despiked using a rolling-median filter (10-point window) that removes points deviating from the local median by more than five times the local median absolute deviation. All NIST 610 analyses of a session are then converted to time-resolved sensitivity profiles, aligned on a common time axis, and averaged, and a sixth-order polynomial is fitted to the session-average profile. This yields a single, time-resolved (i.e. downhole-resolved) sensitivity curve per element that corrects the downhole signal evolution of the standard, while the spread of the per-analysis median sensitivities provides the standard error used in the uncertainty propagation. Uncorrected (pseudo-) concentrations for the unknown are then calculated at each time step as:

$$C_i^{\mathrm{raw}}(t) = \frac{\mathrm{CPS}_i^{\mathrm{sample}}(t)}{S_i(t)} \tag{B3}$$

A residual downhole fractionation correction is applied at this stage: the relative concentration profiles of each element are normalized to their near-surface values, combined point-wise by the median, and a surface-anchored sixth-order polynomial is fitted to the combined profile. The resulting element-specific correction curve multiplies the sensitivity at each depth step.

Rather than converting every element to its simple oxide, each element is assigned a component factor f_i that converts the element mass to the mass of the full stoichiometric compound it represents in the expected mineral assemblage. For elements hosted in oxide-forming phases, this factor is the conventional oxide-to-cation mass ratio (e.g., $f_{\mathrm{Si}} = M_{\mathrm{SiO_2}} / M_{\mathrm{Si}} = 2.139$; $f_{\mathrm{Zr}} = M_{\mathrm{ZrO_2}} / M_{\mathrm{Zr}} = 1.351$). Elements diagnostic of non-oxide minerals on the other hand are used to completely reconstruct the mineral's stoichiometry. Calcium, for example, serves as the only measurable proxy for apatite [$Ca_5(PO_4)_3F$], a common inclusion in zircon and a significant host of the parent nuclides U, Th, and Sm. Phosphorus and fluorine are difficult to quantify by ICP-MS due to high first-ionization potentials, polyatomic interferences (e.g., $^{15}N^{16}O^+$, $^{40}Ar^{19}F^+$), and low sensitivity. We circumvent this limitation by assigning Ca a component factor that reconstructs the entire apatite formula unit from the Ca measurement alone:

$$f_{\mathrm{Ca}} = \frac{M_{\mathrm{Ca_5(PO_4)_3F}}}{5M_{\mathrm{Ca}}} = \frac{504.3}{5 \times 40.078} \approx 2.517 \tag{B4}$$

https://doi.org/10.5194/egusphere-2026-4367
Preprint. Discussion started: 12 August 2026

This means that when Ca is detected, its contribution to the total mass sum includes not only the calcium itself but also the stoichiometrically required phosphate and fluorine. The complete list of elements measured was selected to capture the dominant mass-contributing components of zircon (Si, Zr, Hf), apatite (Ca), rutile (Ti), aluminosilicate phases (Al), iron-bearing phases (Fe), and the parent/daughter nuclides required for (U-Th)/He dating (U, Th, Sm).

Mineral phase proportions are reported at each time step (e.g., "Zircon %", "Apatite %") and are derived after concentration calculation by grouping the component masses by their associated elements:

$$\phi_{\text{phase}}(t) = \frac{\sum_{i \in \text{phase}} C_i^{\text{raw}}(t) f_i}{M_{\text{total}}(t)} \times 100 \tag{B5}$$

Because Si is a structural component of zircon and several common inclusion phases, it cannot serve as a standalone phase indicator in the way that Ca (apatite) or Ti (rutile) can. Instead, the total measured Si (in moles) is reduced by the maximum stoichiometrically plausible Si consumption of every other detected element (1:1 for Zr and Hf (zircon), 1:1 for Ti (titanite), 3:1 for Al (aluminosilicates)) and any remaining Si is converted to SiO_2 and expressed as a mass percentage as "Excess SiO_2". A positive value is a lower bound on the true free SiO_2 fraction, indicating quartz inclusions or an overestimate of Si in the ablation volume. A negative value indicates the presence of Si-free minerals (e.g., corundum rather than feldspar for an Al-bearing inclusion) or a mass-dependent sensitivity drift where Si is underreported relative to heavier elements.

There are two plausible scenarios where our routine can produce inaccurate results: In the case that an inclusion contains elements not in the analyte list, the unmeasured mass will proportionally overestimate the measured elements' concentrations. The bias on U/Th concentrations consequently scales with the mass fraction of the invisible component and is negligible (<1 %) for most common inclusions at realistic proportions (<5 % of the ablation volume). Secondly, measured Ca assigned the apatite factor while present as a simple oxide will result in underestimation of the final element concentrations. This underestimation is largely irrelevant as well when measuring zircons, as errors remain below 0.1 % for Ca concentrations typical of zircon (<1,000 ppm) and only exceed 1 % when CaO constitutes more than ∼1 wt % of the total measured mass. Even at ∼7 wt % CaO present in minerals besides apatite, the error only reaches ∼5 %. Such high concentrations are unlikely, as other Ca-bearing phases (such as anorthite, grossular, or hornblende) only rarely occur as inclusions in zircons and can be identified by other tracer elements if necessary.

Short-timescale analytical noise is estimated using the Mean Squared Successive Differences (MSSD) method (von Neumann et al., 1941), which isolates analytical noise from real compositional variation (zonation) in the depth profile. For n successive concentration measurements $y_1, y_2, \ldots, y_n$ within the signal window, the noise standard deviation is estimated as:

$$\widehat{\sigma}_{\text{noise}} = \frac{\text{SD}(\Delta y_k)}{\sqrt{2}}, \qquad \Delta y_k = y_{k+1} - y_k \tag{B6}$$

where SD is the sample standard deviation of the first differences. The standard error of the mean is then:

$$\text{SE} = \frac{\widehat{\sigma}_{\text{noise}}}{\sqrt{n}} \tag{B7}$$

https://doi.org/10.5194/egusphere-2026-4367
Preprint. Discussion started: 12 August 2026

Analytical uncertainties on the time-averaged concentrations are then propagated by a hybrid bootstrap/Monte Carlo scheme (n = 300 replicates), in which the baseline is bootstrapped, signal noise is added parametrically from the MSSD noise estimate, and the interpolated sensitivity is perturbed by its standard error. All uncertainties are reported as 2σ.

For the zonation metrics, the profile of each spot is segmented dynamically: a jump threshold of $3 \times \sigma_{\mathrm{noise}}$ is used to identify points where the concentration changes by more than expected from analytical noise alone. The profile is split at these jump points, and segments shorter than 5 points are discarded as transient spikes. From the means of the remaining statistically distinct zones, the two metrics are computed: the "Zonation Magnitude" is the ratio of the maximum to the minimum zone mean, providing a measure of the amplitude of zonation relative to analytical scatter (values near 0 mean flat or noisy data, and larger values mean stronger zoning), and the "Zonation Erraticness" is calculated as the total variation (sum of absolute differences between successive zone means) divided by the overall amplitude range (i.e. max − min).

B4 Parent-source depth weighting: Monte Carlo implementation

The reverse Monte Carlo simulation used to depth weight the measured parent concentration consists of: (1) Randomly picking an endpoint location within the He pit of radius R and depth D. A uniform distribution is achieved by sampling the depth z uniformly on $[0,\ D]$, the azimuth φ uniformly on $[0,\ 2\pi]$, and the radial coordinate ρ via the inverse transform $\rho = R \cdot \sqrt{U}$, where U is uniform on [0, 1]. The use of $\sqrt{U}$ is essential, as simply drawing ρ uniformly on $[0,\ R]$ would oversample the centre of the cylinder. Cartesian coordinates are then recovered as:

$$x_0 = \rho\cos(\varphi), \quad y_0 = \rho\sin(\varphi), \quad z_0 = DU_z \tag{B8}$$

(2) Drawing an alpha-ejection path by selecting an isotropic direction and a stopping distance s, with s sampled according to the decay-chain-specific alpha energies and branching probabilities of Ketcham et al. (2011). Each alpha-emitting nuclide of a chain is simulated separately, with its stopping distance drawn from the discrete alpha lines of that emitter according to their branching probabilities; the resulting distributions of stopping distances for all four decay chains are shown in Fig. B1. A truly isotropic direction on the unit sphere is generated using two independent random variables: the directional azimuth ϕ_{dir}, sampled uniformly on $[0, 2\pi]$, and $\mu = cos(\theta)$, sampled uniformly on $[-1, 1]$. Sampling μ, rather than θ itself, avoids overrepresenting directions near the poles. The Cartesian unit vector is then given by:

$$\begin{aligned} u_x &= \sqrt{1-\mu^2}\cos(\varphi_{\mathrm{dir}}), \\ u_y &= \sqrt{1-\mu^2}\sin(\varphi_{\mathrm{dir}}), \\ u_z &= \mu \end{aligned} \tag{B9}$$

(3) Computing the parent location by reversing the alpha trajectory (i.e. the parent sits at the He endpoint plus the alpha ejection vector in the opposite direction):

https://doi.org/10.5194/egusphere-2026-4367
Preprint. Discussion started: 12 August 2026

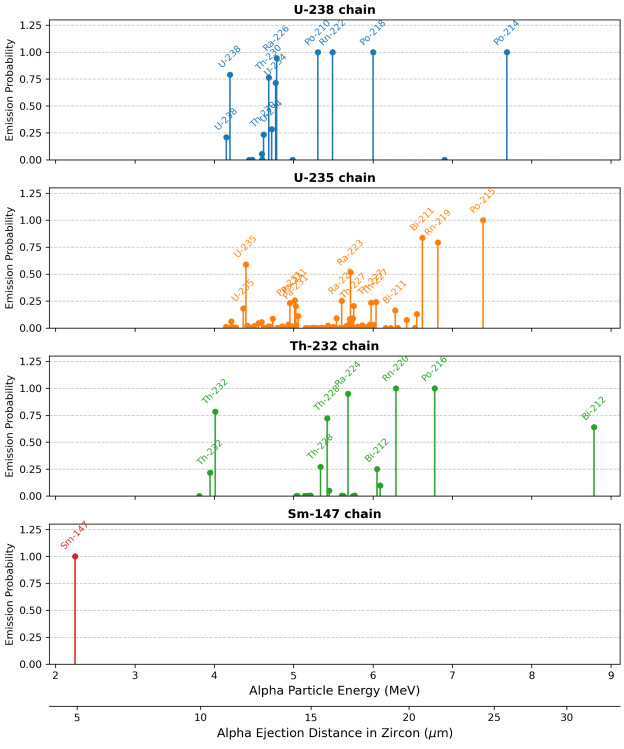

Figure B1. Distributions of alpha particle energies and stopping distances in zircon for the four decay chains.

$$x_p = x_0 - su_x, \quad y_p = y_0 - su_y, \quad z_p = z_0 - su_z \tag{B10}$$

While a more complex infinite-cylinder model might match the geometry of a zircon even more closely, the LA-ICP-MS profile cannot resolve lateral concentration gradients due to substantially better depth resolution than lateral resolution (a 60 μm spot averages over the full lateral extent of the pit but has a typical depth resolution of <0.5 μm). Under the layered-cake assumption described in the main text, the normalized depth-weighting density $w(z)$ is constructed by reducing every parent endpoint coordinate z (ignoring the lateral coordinates x and y), and the resulting set of z values is binned into a histogram with uniform bin width Δz:

$$N_k = \#\left\{ i : z_k - \frac{\Delta z}{2} \le z_i < z_k + \frac{\Delta z}{2} \right\} \tag{B11}$$

where N_k is the count of parent endpoints falling in the k-th bin centred at z_k, and z_i is the depth of the i-th parent endpoint. In practice, the bin width Δz is set to the depth resolution of the ICP-MS profile, obtained by measuring the ICP-MS pit depth D_{ICPMS} on the interferometer and dividing it by the total laser shot count. The histogram is then converted to a normalized probability density by dividing by both the total number of endpoints and the bin width:

https://doi.org/10.5194/egusphere-2026-4367
Preprint. Discussion started: 12 August 2026

$$w(z_k) = \frac{N_k}{\Delta z \sum_j N_j} \tag{B12}$$

The resulting curve is the probability distribution that a randomly selected He atom inside the pit was produced by a parent located at depth z. 200,000 parent decays per chain per emitter are sufficient to get a smooth weighting curve which increases the concentration calculation by only a few seconds per spot. Separate probability profiles are computed for each decay chain, and the combined U curve is obtained by summing the ^{238}U and ^{235}U chain histograms weighted by their isotopic abundance and decay constant before applying the final normalization. For each simulated geometry, the code additionally tallies the fractions of parent endpoints located in the polished-away volume above the grain surface (z < 0) and inside the He pit cavity itself. Examples of the resulting probability clouds and weighting curves for a range of pit diameters and depths, complementing Fig. 4 of the main text, are shown in Fig. B2.

B5 U-Pb age calculation

Optionally, our data reduction code can calculate a U-Pb age in addition to the (U-Th)/He age, providing all necessary isotopes were measured. GJ-1 zircon is used as the primary standard, with an accepted ^{206}Pb/^{238}U age of 601.7 Ma (Jackson et al., 2004). For each GJ-1 analysis in the session, blank-corrected ^{206}Pb and ^{238}U signals are time-integrated over the same region of interest (ROI) used for the unknowns, and a raw ^{206}Pb/^{238}U ratio is calculated. A per-standard fractionation factor is then defined as the ratio of the theoretical GJ-1 ^{206}Pb/^{238}U value, computed from its accepted age and the ^{238}U decay constant (λ_{238} = 1.55125 × 10^{-10} yr^{-1}; Jaffey et al., 1971), to the measured raw ratio. Analogous to the treatment of the NIST 610 sensitivities, a time-resolved fractionation-factor profile is computed for each GJ-1 analysis, the profiles of a session are averaged on a common time axis, and a sixth-order polynomial is fitted to the session-average profile. The raw ^{206}Pb/^{238}U ratio of each unknown is then multiplied by the session-mean fractionation factor, with the standard error of the per-analysis fractionation factors propagated as a systematic uncertainty, to yield the corrected ratio, which is then converted to an age via the standard decay equation:

$$t_{206/238} = \frac{1}{\lambda_{238}} \ln\left(1 + \frac{^{206}\mathrm{Pb}}{^{238}\mathrm{U}}\right) \tag{B13}$$

https://doi.org/10.5194/egusphere-2026-4367
Preprint. Discussion started: 12 August 2026

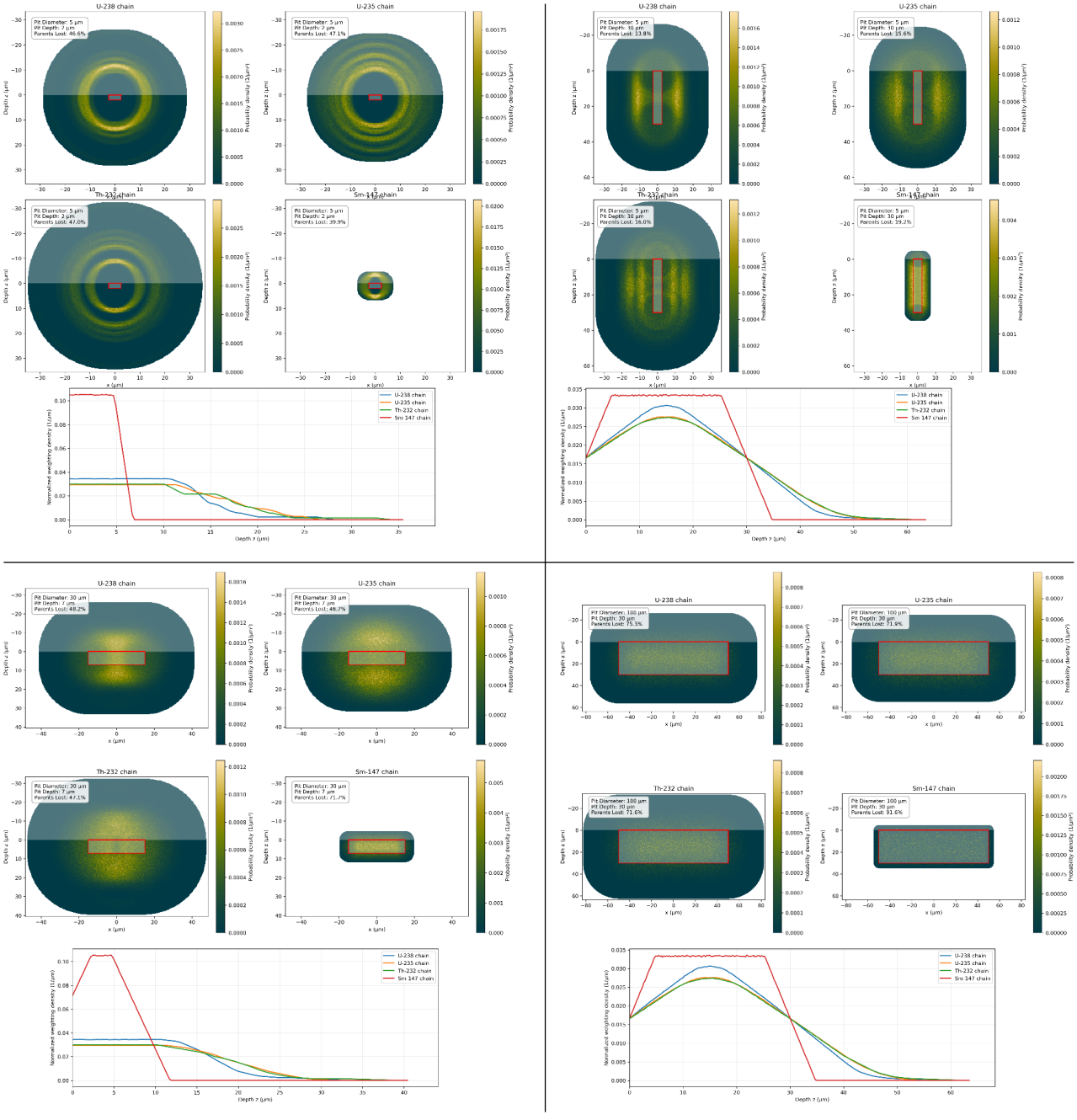

Figure B2. Parent-source probability clouds and depth-weighting curves for a range of pit diameters and depths. Note that a narrow but deep pit (upper right) minimizes the percentage of parents lost, while parents and 4He are much more decoupled in a pit that is both significantly wider and deeper than the ejection distances. At larger spot sizes, the depth weighting correction also becomes more significant.

https://doi.org/10.5194/egusphere-2026-4367
Preprint. Discussion started: 12 August 2026

Appendix C: µ-CT benchmarking of interferometric pit volumes

Many of the possible problems with the commonly used methods to measure ablation pit volumes result from measurements being taken from only one direction (looking down the ablated hole). This makes irregular shapes within the crater (e.g. overhanging / steep slopes or dust particles) difficult to image. X-ray micro-computed tomography (µ-CT), on the other hand, can reconstruct the pit geometry in three dimensions and differentiate materials based on X-ray attenuation, thereby potentially avoiding such issues. µ-CT is therefore ideally suited to test the accuracy of our interferometer volume measurements over a wide range of pit depths and pit diameters.

We ablated a total of 291 test pits over three runs in polished gem-quality Sri Lanka zircon megacrysts with laser spot diameters varying from 5 to 150 µm and depths ranging from 1 to 50 µm. The volumes were first measured on the interferometer using the above protocol. Subsequently, the volume was measured again using µ-CT. To reduce "beam-hardening" artifacts, caused by preferential absorption of lower-energy photons from the polychromatic X-ray beam (Bam et al., 2019), the ablated zircon slab was covered with a thicker polished zircon slab that acted as a material-matched prefilter and "hardened" the beam before it reached the sample. After a low-resolution exploratory scan, the pits were scanned on a Zeiss Xradia 620 Versa at 160 kV, with a voxel size of 1.02 µm for the first run, and 3.41 µm for the subsequent two runs. For each run, a total of 999 projections were taken, each with an exposure time of 24 s. The lower resolution of µ-CT compared to white-light interferometry makes imaging small features challenging. If, as for this study, the goal is not to get a precise geometry of a feature, but a total volume, this pitfall can be overcome by the partial volume blurring (PVB) method (Ketcham and Mote, 2019). The PVB approach makes use of the fact that features at or below the resolution limit are blurred by the data point-spread function (PSF). If the CT numbers of two endmembers (in this case zircon and air) are known, a partial volume of each material can be calculated and summed up across the blurred region. If these conditions are met, the method is able to give accurate volume measurements independent of the resolution or feature size. Even with the material-matched prefilter, residual beam hardening causes a systematic increase of CT numbers towards the middle of the sample, which interfered with the precise measurement of greyscale values. To remove this artifact, we developed a Python routine that corrects the background grayscale values of each slice: the dataset is first re-oriented such that the slices are perpendicular to the ablated pits, and a set of 16 profiles running through zircon is defined over each slice. A polynomial function is fitted to the grayscale values along each profile, the profile fits are interpolated across a grid of the same size as the original CT image, and a correction matrix is calculated by dividing each value of the interpolated fit by the average grayscale value of the dataset. Applying this correction matrix to the original CT images removes the systematic variation in the grayscale values of zircon across each slice while preserving noise and primary features.

The volume of each pit was then extracted from the corrected dataset using the PVB implementation in the Blob3D software package (Ketcham, 2005). The method requires the CT numbers of the two endmember materials. The CT number of zircon was determined by manually sampling areas surrounding the pits, while the CT number of air inside the pits depends on the degree of blurring. The extent of blurring in each dataset was therefore assessed by fitting the point-spread function (PSF) through the contact between the polished cover zircon and the pit air, which represents a pure blurring profile unaltered by

https://doi.org/10.5194/egusphere-2026-4367
Preprint. Discussion started: 12 August 2026

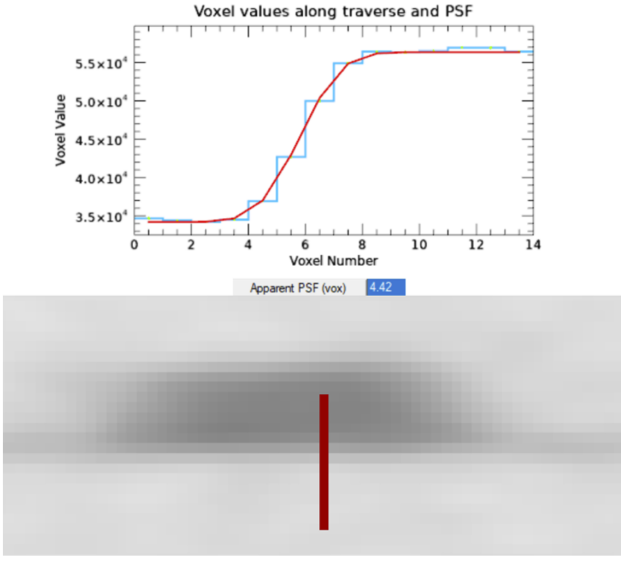

Figure C1. The profile through the zircon cover and ablated pit (lower), while in the real world a sharp contact, is blurred in the CT image. Fitting a PSF curve through the blurred region (upper) gives a value of 4.43 ± 0.35 µm. The profile is 14 µm long.

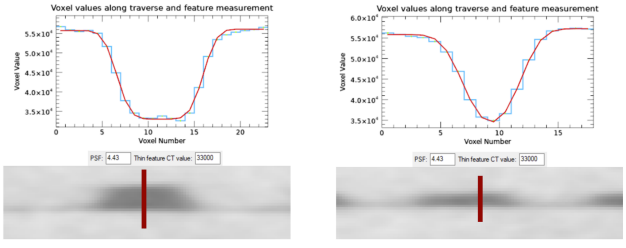

Figure C2. Profiles through deep (left) and shallow (right) pits. Modelled blurred profiles with a PSF value of 4.43 and a CTAir number of 33000 fit both pits well.

surface roughness (Fig. C1). For pits large enough to contain unblurred air, the measured CT number of air can be used directly; for smaller and shallower pits, theoretical blurred profiles across the entire pit were modelled using the measured PSF to derive a consistent CT number of air (Fig. C2). The pits were then segmented using a threshold chosen to include the surrounding zircon, as any extra volume of pure zircon does not contribute partial air volume to the result, and all segmented blobs were manually checked to ensure that all pits, and no other features, were included.

https://doi.org/10.5194/egusphere-2026-4367
Preprint. Discussion started: 12 August 2026

Appendix D: Machine-learning model

D1 Implementation details

The machine-learning analysis was implemented in Python using *scikit-learn* and SHAP. The response variable was the signed age residual relative to the accepted Fish Canyon Tuff reference age of 28.30 Ma:

$$r_i = t_i - 28.30\ \mathrm{Ma} \tag{D1}$$

such that positive residuals represent ages older than the reference value. Age, age uncertainty, analysis identifiers, and the directly age-defining ^{4}He, ^{238}U, and ^{232}Th concentrations were excluded from the predictor set to prevent target leakage.

Age residuals were modeled using a HistGradientBoostingRegressor with a maximum tree depth of 6, a learning rate of 0.05, and 900 boosting iterations. Model performance was assessed by ten-fold out-of-fold cross-validation repeated ten times using shuffled partitions. Each analysis therefore received one independent prediction per repeat, and the final per-spot prediction was calculated as the mean of these ten predictions. Explained variance was calculated as

$$1 - \frac{\mathrm{Var}(r - \hat{r})}{\mathrm{Var}(r)} \tag{D2}$$

and remaining dispersion was summarized using the median absolute deviation scaled by 1.4826.

Feature importance was assessed independently using a fixed 80:20 training-holdout split. Permutation importance was defined as the mean decrease in holdout-set R^2 after individually shuffling each predictor 30 times. SHAP values were calculated from fold-specific models and aggregated to the original predictor level, providing feature contributions in Ma. The unique contribution of broader parameter groups was tested by leave-one-group-out analysis, in which the complete model was compared with models refitted after removing each group. Feature stability was evaluated across 50 repeated half-sample fits and expressed as the fraction of runs in which permutation importance remained positive. Finally, shuffled-target analyses were used to establish the predictive performance and feature stability expected by chance. Together, these complementary diagnostics distinguish variables that are only correlated with age residuals from those that provide reproducible predictive information.

https://doi.org/10.5194/egusphere-2026-4367
Preprint. Discussion started: 12 August 2026

D2 Model results

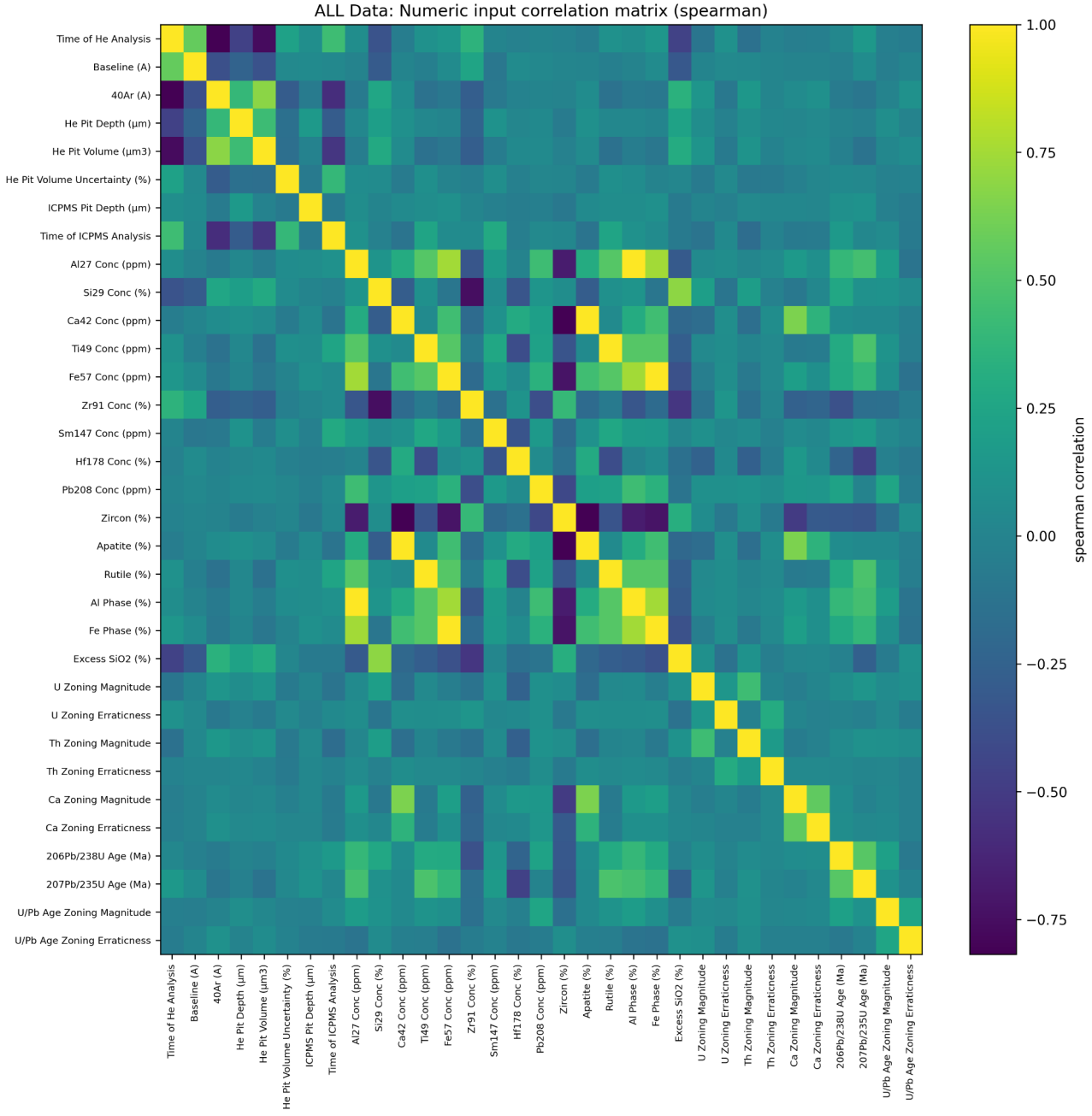

Figure D1. Spearman correlation of all target parameters of the ML model.

https://doi.org/10.5194/egusphere-2026-4367
Preprint. Discussion started: 12 August 2026

Table D1. Feature-level permutation importance, bootstrap stability, and mean |SHAP| for all 33 candidate predictors used in the HistGradientBoosting dispersion model. Shaded rows are group-level: LOGO $\Delta\sigma_{\mathrm{MAD}}$ (Ma) is the increase in unexplained out-of-fold scatter when the entire group is removed from the model, and PI (ΔR^2) is the summed permutation importance of the group's features. Unshaded rows give per-feature values: PI (ΔR^2) is the decrease in OOF variance explained when that feature alone is shuffled (mean ± SD over repeated CV). Stability is the fractions of bootstrap refits in which the feature is retained as predictive by the permutation-importance (GBR) stability criteria. Mean |SHAP| (Ma) is the absolute per-spot contribution of the feature to the predicted age residual, averaged over all spots. "Robust" (✓) marks features meeting both stability criteria at the 0.6 threshold.

Group or feature	LOGO $\Delta\sigma_{\mathrm{MAD}}$ (Ma)	PI (ΔR^2)	Stability	Mean |SHAP| (Ma)	Robust
Geometry / ablation	**+0.371**	**+0.337**	–	–	–
He pit volume (μm^3)	–	+0.343 ± 0.061	1.00	1.445	✓
He pit depth (μm)	–	+0.009 ± 0.011	0.80	0.273	✓
ICP-MS pit depth (μm)	–	−0.007 ± 0.013	0.76	0.214	–
He pit volume uncertainty (%)	–	−0.008 ± 0.008	0.50	0.168	–
ICP-MS chemistry	**+0.181**	**+0.050**	–	–	–
^{208}Pb concentration (ppm)	–	+0.047 ± 0.023	1.00	0.769	✓
^{178}Hf concentration (%)	–	+0.009 ± 0.010	0.76	0.221	✓
^{91}Zr concentration (%)	–	+0.009 ± 0.009	0.54	0.167	–
^{42}Ca concentration (ppm)	–	+0.006 ± 0.004	0.66	0.196	–
^{29}Si concentration (%)	–	+0.005 ± 0.006	0.58	0.223	–
^{147}Sm concentration (ppm)	–	+0.000 ± 0.008	0.88	0.184	✓
^{49}Ti concentration (ppm)	–	−0.001 ± 0.009	0.52	0.212	–
^{57}Fe concentration (ppm)	–	−0.005 ± 0.006	0.52	0.158	–
^{27}Al concentration (ppm)	–	−0.019 ± 0.006	0.44	0.179	–
Mineralogy fractions	**+0.039**	**−0.008**	–	–	–
Excess SiO_2 (%)	–	+0.001 ± 0.004	0.38	0.095	–
Rutile (%)	–	+0.000 ± 0.000	0.00	0.000	–
Apatite (%)	–	+0.000 ± 0.000	0.00	0.000	–
Al phase (%)	–	+0.000 ± 0.000	0.00	0.000	–
Fe phase (%)	–	+0.000 ± 0.000	0.00	0.000	–
Zircon (%)	–	−0.008 ± 0.007	0.58	0.199	–
Zonation	**+0.003**	**+0.046**	–	–	–
Ca zoning magnitude	–	+0.023 ± 0.011	0.82	0.180	✓
Th zoning magnitude	–	+0.016 ± 0.007	0.52	0.137	–
Th zoning erraticness	–	+0.016 ± 0.009	0.80	0.259	✓
U zoning erraticness	–	+0.014 ± 0.019	0.92	0.366	✓
Ca zoning erraticness	–	−0.003 ± 0.007	0.68	0.116	✓
U zoning magnitude	–	−0.021 ± 0.008	0.70	0.168	–
QMS / He signals	**−0.034**	**+0.065**	–	–	–
Baseline (A)	–	+0.063 ± 0.033	0.96	0.466	✓
^{40}Ar (A)	–	+0.001 ± 0.007	0.66	0.203	–
U–Pb context	**−0.098**	**+0.088**	–	–	–
^{206}Pb/^{238}U age (Ma)	–	+0.072 ± 0.014	0.72	0.381	✓
^{207}Pb/^{235}U age (Ma)	–	+0.018 ± 0.010	0.90	0.401	✓
U–Pb age zoning erraticness	–	+0.005 ± 0.008	0.66	0.147	✓
U–Pb age zoning magnitude	–	−0.007 ± 0.005	0.20	0.131	–
Time / session	**−0.106**	**+0.015**	–	–	–
Time of ICP-MS analysis	–	+0.012 ± 0.009	0.64	0.144	✓
Time of He analysis	–	+0.003 ± 0.005	0.64	0.122	–

https://doi.org/10.5194/egusphere-2026-4367
Preprint. Discussion started: 12 August 2026

Code and data availability. The Python codes for helium data reduction, pit-volume extraction, oxide-sum normalization, parent-source depth weighting, the dispersion-attribution model and the complete dataset used for the analysis are available on Zenodo at https://doi.org/10.5281/zenodo.21446630 (Ehrenfels, 2026).

Author contributions. MKE developed the analytical workflow, data-reduction software, the dispersion ML model, performed the analyses, and wrote the manuscript. DFS supervised the study. RAK contributed to the μ-CT analyses and alpha-stopping calculations. DBP contributed to the extraction-line design and He measurements. MGP contributed to the sample preparation setup. All authors discussed the results and edited the manuscript.

Competing interests. The authors declare that they have no conflict of interest.

Acknowledgements. The author would like to thank Lisa Stockli and Rudra Chatterjee for their assistance and training in the lab. Jessie Maisano is thanked for her help with the μ-CT measurements. Pieter Vermeesch is thanked for his helpful comments and discussion of the manuscript.

Financial support. This study was supported by the UTChron lab and the Geological Society of America through a Graduate Student Research Grant to MKE. MKE was supported through the Mark Cloos Endowed Graduate Fellowship and the Bookout Endowed Chair in Structural Geology of the Jackson School of Geoscience.

https://doi.org/10.5194/egusphere-2026-4367
Preprint. Discussion started: 12 August 2026

References

Bam, L. C., Miller, J. A., Becker, M., and Basson, I. J.: X-ray computed tomography: Practical evaluation of beam hardening in iron ore samples, Miner. Eng., 131, 206–215, https://doi.org/10.1016/j.mineng.2018.11.010, 2019.

Bleiner, D. and Bogaerts, A.: Multiplicity and contiguity of ablation mechanisms in laser-assisted analytical micro-sampling, Spectrochim. Acta B, 61, 421–432, https://doi.org/10.1016/j.sab.2006.02.007, 2006.

Boyce, J. W., Hodges, K. V., Olszewski, W. J., Jercinovic, M. J., Carpenter, B. D., and Reiners, P. W.: Laser microprobe (U-Th)/He geochronology, Geochim. Cosmochim. Ac., 70, 3031–3039, https://doi.org/10.1016/j.gca.2006.03.019, 2006.

Coupland, J. M. and Lobera, J.: Measurement of steep surfaces using white light interferometry, Strain, 46, 69–78, https://doi.org/10.1111/j.1475-1305.2008.00595.x, 2010.

Danišík, M., McInnes, B. I. A., Kirkland, C. L., McDonald, B. J., Evans, N. J., and Becker, T.: Seeing is believing: Visualization of He distribution in zircon and implications for thermal history reconstruction on single crystals, Sci. Adv., 3, e1601121, https://doi.org/10.1126/sciadv.1601121, 2017.

Diaz, A. F. and Felix-Navarro, R. M.: A semi-quantitative tribo-electric series for polymeric materials: The influence of chemical structure and properties, J. Electrostat., 62, 277–290, https://doi.org/10.1016/j.elstat.2004.05.005, 2004.

Dobson, K. J., Stuart, F. M., Dempster, T. J., and EIMF: U and Th zonation in Fish Canyon Tuff zircons: Implications for a zircon (U-Th)/He standard, Geochim. Cosmochim. Ac., 72, 4745–4755, https://doi.org/10.1016/j.gca.2008.07.015, 2008.

Ehrenfels, M. K.: Code and data for "Analytical improvements and a machine-learning assessment of age dispersion in laser-ablation (U-Th)/He zircon dating", version 1.01, Zenodo [code and data], https://doi.org/10.5281/zenodo.21446630, 2026.

Evans, N. J., McInnes, B. I. A., McDonald, B., Danišík, M., Becker, T., Vermeesch, P., Shelley, M., Marillo-Sialer, E., and Patterson, D. B.: An in situ technique for (U-Th-Sm)/He and U-Pb double dating, J. Anal. At. Spectrom., 30, 1636–1645, https://doi.org/10.1039/C5JA00085H, 2015.

Farley, K. A.: (U-Th)/He dating: Techniques, calibrations, and applications, Rev. Mineral. Geochem., 47, 819–844, https://doi.org/10.2138/rmg.2002.47.18, 2002.

Flowers, R. M., Zeitler, P. K., Danišík, M., Reiners, P. W., Gautheron, C., Ketcham, R. A., Metcalf, J. R., Stockli, D. F., Enkelmann, E., and Brown, R. W.: (U-Th)/He chronology: Part 1. Data, uncertainty, and reporting, Geol. Soc. Am. Bull., 135, 104–136, https://doi.org/10.1130/B36266.1, 2023a.

Flowers, R. M., Ketcham, R. A., Enkelmann, E., Gautheron, C., Reiners, P. W., Metcalf, J. R., Danišík, M., Stockli, D. F., and Brown, R. W.: (U-Th)/He chronology: Part 2. Considerations for evaluating, integrating, and interpreting conventional individual aliquot data, Geol. Soc. Am. Bull., 135, 137–161, https://doi.org/10.1130/B36268.1, 2023b.

Fryer, B. J., Jackson, S. E., and Longerich, H. P.: The application of laser ablation microprobe-inductively coupled plasma-mass spectrometry (LAM-ICP-MS) to in situ (U)-Pb geochronology, Chem. Geol., 109, 1–8, https://doi.org/10.1016/0009-2541(93)90058-Q, 1993.

Gagnon, J. E., Fryer, B. J., Samson, I. M., and Williams-Jones, A. E.: Quantitative analysis of silicate certified reference materials by LA-ICPMS with and without an internal standard, J. Anal. At. Spectrom., 23, 1529–1537, https://doi.org/10.1039/B801807N, 2008.

Gehrels, G. E., Valencia, V. A., and Ruiz, J.: Enhanced precision, accuracy, efficiency, and spatial resolution of U-Pb ages by laser ablation-multicollector-inductively coupled plasma-mass spectrometry, Geochem. Geophys. Geosyst., 9, Q03017, https://doi.org/10.1029/2007GC001805, 2008.

https://doi.org/10.5194/egusphere-2026-4367
Preprint. Discussion started: 12 August 2026

Gleadow, A., Harrison, M., Kohn, B., Lugo-Zazueta, R., and Phillips, D.: The Fish Canyon Tuff: A new look at an old low-temperature thermochronology standard, Earth Planet. Sci. Lett., 424, 95–108, https://doi.org/10.1016/j.epsl.2015.05.003, 2015.

Glotzbach, C. and Ehlers, T. A.: Interpreting cooling dates and histories from laser ablation in situ (U-Th-Sm)/He thermochronometry: A modelling perspective, Geochronology, 6, 697–717, https://doi.org/10.5194/gchron-6-697-2024, 2024.

Gray, A. L.: Solid sample introduction by laser ablation for inductively coupled plasma source mass spectrometry, Analyst, 110, 551–556, https://doi.org/10.1039/AN9851000551, 1985.

Guillong, M., Hametner, K., Reusser, E., Wilson, S. A., and Günther, D.: Preliminary characterisation of new glass reference materials (GSA-1G, GSC-1G, GSD-1G and GSE-1G) by laser ablation-inductively coupled plasma-mass spectrometry using 193 nm, 213 nm and 266 nm wavelengths, Geostand. Geoanal. Res., 29, 315–331, https://doi.org/10.1111/j.1751-908X.2005.tb00903.x, 2005.

Halicz, L. and Günther, D.: Quantitative analysis of silicates using LA-ICP-MS with liquid calibration, J. Anal. At. Spectrom., 19, 1539–1545, https://doi.org/10.1039/B410132D, 2004.

Hao, Y., Wang, Y., Zhang, Z., Yu, J., Wang, Y., Pang, J., Zhang, W., and Zheng, D.: Advancing (U-Th)/He zircon dating: Novel approaches in sample preparation and uncertainty reduction, Lithosphere, 2023, lithosphere_2023_258, https://doi.org/10.2113/2023/lithosphere_2023_258, 2024.

Hiess, J., Condon, D. J., McLean, N., and Noble, S. R.: 238U/235U systematics in terrestrial uranium-bearing minerals, Science, 335, 1610–1614, https://doi.org/10.1126/science.1215507, 2012.

Hodges, K. V., Ruhl, K. W., Wobus, C. W., and Pringle, M. S.: 40Ar/39Ar thermochronology of detrital minerals, Rev. Mineral. Geochem., 58, 239–257, https://doi.org/10.2138/rmg.2005.58.9, 2005.

Hodges, K. V., van Soest, M. C., and McKanna, A. J.: The continuing evolution of laser ablation (U-Th)/He methods: From dates to intracrystalline isotopic distributions, 17th International Conference on Thermochronology, Santa Fe, New Mexico, USA, 12–17 September 2021, https://doi.org/10.1002/essoar.10507946.1, 2021.

Holland, H. D. and Gottfried, D.: The effect of nuclear radiation on the structure of zircon, Acta Crystallogr., 8, 291–300, https://doi.org/10.1107/S0365110X55000947, 1955.

Horn, I., Rudnick, R. L., and McDonough, W. F.: Precise elemental and isotope ratio determination by simultaneous solution nebulization and laser ablation-ICP-MS: Application to U-Pb geochronology, Chem. Geol., 164, 281–301, https://doi.org/10.1016/S0009-2541(99)00168-0, 2000.

Horne, A. M., van Soest, M. C., Hodges, K. V., Tripathy-Lang, A., and Hourigan, J. K.: Integrated single crystal laser ablation U/Pb and (U-Th)/He dating of detrital accessory minerals—Proof-of-concept studies of titanites and zircons from the Fish Canyon Tuff, Geochim. Cosmochim. Ac., 178, 106–123, https://doi.org/10.1016/j.gca.2015.11.044, 2016.

Horne, A. M., van Soest, M. C., and Hodges, K. V.: U/Pb and (U-Th-Sm)/He "double" dating of detrital apatite by laser ablation: A critical evaluation, Chem. Geol., 506, 40–50, https://doi.org/10.1016/j.chemgeo.2018.12.004, 2019.

Hourigan, J. K., Reiners, P. W., and Brandon, M. T.: U-Th zonation-dependent alpha-ejection in (U-Th)/He chronometry, Geochim. Cosmochim. Ac., 69, 3349–3365, https://doi.org/10.1016/j.gca.2005.01.024, 2005.

Jackson, S. E., Pearson, N. J., Griffin, W. L., and Belousova, E. A.: The application of laser ablation-inductively coupled plasma-mass spectrometry to in situ U-Pb zircon geochronology, Chem. Geol., 211, 47–69, https://doi.org/10.1016/j.chemgeo.2004.06.017, 2004.

Jaffey, A. H., Flynn, K. F., Glendenin, L. E., Bentley, W. C., and Essling, A. M.: Precision measurement of half-lives and specific activities of ^{235}U and ^{238}U, Phys. Rev. C, 4, 1889–1906, https://doi.org/10.1103/PhysRevC.4.1889, 1971.

https://doi.org/10.5194/egusphere-2026-4367
Preprint. Discussion started: 12 August 2026

Jochum, K. P., Weis, U., Stoll, B., Kuzmin, D., Yang, Q., Raczek, I., Jacob, D. E., Stracke, A., Birbaum, K., Frick, D. A., Günther, D., and Enzweiler, J.: Determination of reference values for NIST SRM 610–617 glasses following ISO guidelines, Geostand. Geoanal. Res., 35, 397–429, https://doi.org/10.1111/j.1751-908X.2011.00120.x, 2011.

Kelley, S. P., Arnaud, N. O., and Turner, S. P.: High spatial resolution 40Ar/39Ar investigations using an ultra-violet laser probe extraction technique, Geochim. Cosmochim. Ac., 58, 3519–3525, https://doi.org/10.1016/0016-7037(94)90103-1, 1994.

Kennedy, A. K., Wotzlaw, J.-F., Schaltegger, U., Crowley, J. L., and Schmitz, M. D.: Eocene zircon reference material for microanalysis of U-Th-Pb isotopes and trace elements, Can. Mineral., 52, 409–421, https://doi.org/10.3749/canmin.52.3.409, 2014.

Ketcham, R. A.: Computational methods for quantitative analysis of three-dimensional features in geological specimens, Geosphere, 1, 32–41, https://doi.org/10.1130/GES00001.1, 2005.

Ketcham, R. A., Gautheron, C., and Tassan-Got, L.: Accounting for long alpha-particle stopping distances in (U-Th-Sm)/He geochronology: Refinement of the baseline case, Geochim. Cosmochim. Ac., 75, 7779–7791, https://doi.org/10.1016/j.gca.2011.10.011, 2011.

Ketcham, R. A. and Mote, A. S.: Accurate measurement of small features in X-ray CT data volumes, demonstrated using gold grains, J. Geophys. Res.-Sol. Ea., 124, 3508–3529, https://doi.org/10.1029/2018JB017083, 2019.

Košler, J. and Sylvester, P. J.: Present trends and the future of zircon in geochronology: Laser ablation ICPMS, in: Zircon, edited by: Hanchar, J. M. and Hoskin, P. W. O., Rev. Mineral. Geochem., 53, 243–275, https://doi.org/10.2113/0530243, 2003.

Kramar, N., Cosca, M. A., and Hunziker, J. C.: Heterogeneous 40Ar* distributions in naturally deformed muscovite: In situ UV-laser ablation evidence for microstructurally controlled intragrain diffusion, Earth Planet. Sci. Lett., 192, 377–388, https://doi.org/10.1016/S0012-821X(01)00456-3, 2001.

Kroslakova, I. and Günther, D.: Elemental fractionation in laser ablation-inductively coupled plasma-mass spectrometry: Evidence for mass load induced matrix effects in the ICP during ablation of a silicate glass, J. Anal. At. Spectrom., 22, 51–62, https://doi.org/10.1039/B606522H, 2007.

Léger, J., Pik, R., Tibari, B., Ternois, S., Ford, M., Peiffert, C., and Mercadier, J.: Laser ablation (U-Th-Sm)/He dating of zircons: Analytical age bias and its consequence for studying detrital zircon populations, Geostand. Geoanal. Res., 47, 219–242, https://doi.org/10.1111/ggr.12494, 2023.

Liu, Y., Hu, Z., Gao, S., Günther, D., Xu, J., Gao, C., and Chen, H.: In situ analysis of major and trace elements of anhydrous minerals by LA-ICP-MS without applying an internal standard, Chem. Geol., 257, 34–43, https://doi.org/10.1016/j.chemgeo.2008.08.004, 2008.

Lundberg, S. M. and Lee, S.-I.: A unified approach to interpreting model predictions, in: Advances in Neural Information Processing Systems 30, edited by: Guyon, I., von Luxburg, U., Bengio, S., Wallach, H., Fergus, R., Vishwanathan, S. V. N., and Garnett, R., Curran Associates, Inc., 4765–4774, 2017.

Maier, A. K., Glotzbach, C., and Falkowski, S.: Analytical and modelling strategies for thermal histories from in situ (U-Th-Sm)/He data of single apatites, Geochronology, 8, 165–189, https://doi.org/10.5194/gchron-8-165-2026, 2026.

Martínez Antón, J. C., Alonso, J., and Gómez Pedrero, J. A.: Topographic optical profilometry of steep slope micro-optical transparent surfaces, Opt. Express, 23, 9494–9507, https://doi.org/10.1364/OE.23.009494, 2015.

Murray, K. E., Orme, D. A., and Reiners, P. W.: Effects of U-Th-rich grain boundary phases on apatite helium ages, Chem. Geol., 390, 135–151, https://doi.org/10.1016/j.chemgeo.2014.09.023, 2014.

Pedregosa, F., Varoquaux, G., Gramfort, A., Michel, V., Thirion, B., Grisel, O., Blondel, M., Prettenhofer, P., Weiss, R., Dubourg, V., Vanderplas, J., Passos, A., Cournapeau, D., Brucher, M., Perrot, M., and Duchesnay, É.: Scikit-learn: Machine learning in Python, J. Mach. Learn. Res., 12, 2825–2830, 2011.

https://doi.org/10.5194/egusphere-2026-4367
Preprint. Discussion started: 12 August 2026

Pickering, J., Matthews, W., Enkelmann, E., Guest, B., Sykes, C., and Koblinger, B. M.: Laser ablation (U-Th-Sm)/He dating of detrital apatite, Chem. Geol., 548, 119683, https://doi.org/10.1016/j.chemgeo.2020.119683, 2020.

Reiners, P. W.: Zircon (U-Th)/He thermochronometry, Rev. Mineral. Geochem., 58, 151–179, https://doi.org/10.2138/rmg.2005.58.6, 2005.

Russo, R. E., Mao, X., Gonzalez, J. J., Zorba, V., and Yoo, J.-H.: Laser ablation in analytical chemistry, Anal. Chem., 85, 6162–6177, https://doi.org/10.1021/ac4005327, 2013.

Shaulis, B. J., Lapen, T. J., and Toms, A.: Signal linearity of an extended range pulse counting detector: Applications to accurate and precise U-Pb dating of zircon by laser ablation quadrupole ICP-MS, Geochem. Geophys. Geosyst., 11, Q0AA11, https://doi.org/10.1029/2010GC003198, 2010.

Spiegel, C., Kohn, B. P., Belton, D. X., Berner, Z., and Gleadow, A. J. W.: Apatite (U-Th-Sm)/He thermochronology of rapidly cooled samples: The effect of He implantation, Earth Planet. Sci. Lett., 285, 105–114, https://doi.org/10.1016/j.epsl.2009.05.045, 2009.

Stockli, D. F., Odlum, M., and Patterson, D. B.: UV laser ablation in ultra-high vacuum: Plasma shields and popcorn, in: North American Workshop on Laser Ablation 2017 Abstract Volume, 2017.

Sylvester, P. J.: Matrix effects in laser ablation ICP-MS, in: Laser Ablation ICP-MS in the Earth Sciences: Current Practices and Outstanding Issues, edited by: Sylvester, P. J., Mineralogical Association of Canada Short Course Series, 40, 67–78, https://doi.org/10.3749/9780921294801.ch05, 2008.

Tian, Y., Vermeesch, P., Danišík, M., Condon, D. J., Chen, W., Kohn, B., Schwanethal, J., and Rittner, M.: LGC-1: A zircon reference material for in-situ (U-Th)/He dating, Chem. Geol., 454, 80–92, https://doi.org/10.1016/j.chemgeo.2017.02.026, 2017.

Tripathy-Lang, A., Hodges, K. V., Monteleone, B. D., and van Soest, M. C.: Laser (U-Th)/He thermochronology of detrital zircons as a tool for studying surface processes in modern catchments, J. Geophys. Res.-Earth, 118, 1333–1341, https://doi.org/10.1002/jgrf.20091, 2013.

Van Soest, M. C., Hodges, K. V., Anderson, A. J., Horne, A. M., McDonald, C. S., and Mercer, C. M.: UV laser ablation applications in noble gas analysis, in: North American Workshop on Laser Ablation 2017 Abstract Volume, 2017.

Vermeesch, P., Seward, D., Latkoczy, C., Wipf, M., Günther, D., and Baur, H.: α-Emitting mineral inclusions in apatite, their effect on (U-Th)/He dates, and how to reduce it, Geochim. Cosmochim. Ac., 71, 1737–1746, https://doi.org/10.1016/j.gca.2006.09.020, 2007.

Vermeesch, P., Sherlock, S. C., Roberts, N. M. W., and Carter, A.: A simple method for in-situ U-Th-He dating, Geochim. Cosmochim. Ac., 79, 140–147, https://doi.org/10.1016/j.gca.2011.11.042, 2012.

Vermeesch, P., Tian, Y., Schwanethal, J., and Buret, Y.: Technical note: In situ U-Th-He dating by 4He/3He laser microprobe analysis, Geochronology, 5, 323–332, https://doi.org/10.5194/gchron-5-323-2023, 2023.

von Neumann, J., Kent, R. H., Bellinson, H. R., and Hart, B. I.: The mean square successive difference, Ann. Math. Stat., 12, 153–162, https://doi.org/10.1214/aoms/1177731746, 1941.

Wartho, J.-A., Kelley, S. P., Brooker, R. A., Carroll, M. R., Villa, I. M., and Lee, M. R.: Direct measurement of Ar diffusion profiles in a gem-quality Madagascar K-feldspar using the ultra-violet laser ablation microprobe (UVLAMP), Earth Planet. Sci. Lett., 170, 141–153, https://doi.org/10.1016/S0012-821X(99)00088-6, 1999.

Wolfe, M. R. and Stockli, D. F.: Zircon (U-Th)/He thermochronometry in the KTB drill hole, Germany, and its implications for bulk He diffusion kinetics in zircon, Earth Planet. Sci. Lett., 295, 69–82, https://doi.org/10.1016/j.epsl.2010.03.025, 2010.

Wu, L., Shi, G., Danišík, M., Zhang, Z., Wang, Y., and Wang, F.: MK-1 apatite: A new potential reference material for (U-Th)/He dating, Geostand. Geoanal. Res., 43, 301–315, https://doi.org/10.1111/ggr.12258, 2019.

Zeitler, P. K., Herczeg, A. L., McDougall, I., and Honda, M.: U-Th-He dating of apatite: A potential thermochronometer, Geochim. Cosmochim. Ac., 51, 2865–2868, https://doi.org/10.1016/0016-7037(87)90164-5, 1987.